

# Impact of urban structure on COVID-19 spread

Javier Aguilar,<sup>1</sup> Aleix Bassolas,<sup>2</sup> Gourab Ghoshal,<sup>3,4,\*</sup> Surendra Hazarie,<sup>3</sup> Alec Kirkley,<sup>5</sup> Mattia Mazzoli,<sup>1</sup> Sandro Meloni,<sup>1</sup> Sayat Mimar,<sup>3</sup> Vincenzo Nicosia,<sup>2</sup> José J. Ramasco,<sup>1,†</sup> and Adam Sadilek<sup>6,‡</sup>

<sup>1</sup>*Instituto de Física Interdisciplinar y Sistemas Complejos IFISC (CSIC-UIB), 07122 Palma de Mallorca, Spain.*

<sup>2</sup>*School of Mathematical Sciences, Queen Mary University of London,  
Mile End Road, E1 4NS, London, United Kingdom.*

<sup>3</sup>*Department of Physics & Astronomy, University of Rochester, Rochester, NY, 14627, USA.*

<sup>4</sup>*Department of Computer Science, University of Rochester, Rochester, NY, 14627, USA.*

<sup>5</sup>*Department of Physics, University of Michigan, Ann Arbor, MI, 48109, USA.*

<sup>6</sup>*Google, 1600 Amphitheatre Parkway, Mountain View, CA, 94043, USA.*

(Dated: July 31, 2020)

The ongoing COVID-19 pandemic has created a global crisis of massive scale. Prior research indicates that human mobility is one of the key factors involved in viral spreading [1–10]. Indeed, in a connected planet, rapid world-wide spread is enabled by long-distance air-, land- and sea-transportation among countries and continents, and subsequently fostered by commuting trips within densely populated cities [4, 6, 11–15]. While early travel restrictions contribute to delayed disease spread, their utility is much reduced if the disease has a long incubation period or if there is asymptomatic transmission [16–27]. Given the lack of vaccines, public health officials have mainly relied on non-pharmaceutical interventions, including social distancing measures, curfews, and stay-at-home orders [13, 22–26, 28–32]. Here we study the impact of city organization on its susceptibility to disease spread, and amenability to interventions. Cities can be classified according to their mobility in a spectrum between compact-hierarchical and decentralized-sprawled [33–35]. Our results show that even though hierarchical cities are more susceptible to the rapid spread of epidemics, their organization makes mobility restrictions quite effective. Conversely, sprawled cities are characterized by a much slower initial spread, but are less responsive to mobility restrictions. These findings hold globally across cities in diverse geographical locations and a broad range of sizes. Our empirical measurements are confirmed by a simulation of COVID-19 spread in urban areas through a compartmental model. These results suggest that investing resources on early monitoring and prompt ad-hoc interventions in more vulnerable cities may prove most helpful in containing and reducing the impact of present and future pandemics.

The SARS-CoV-2 virus, believed to have originated in the Hubei province of China around the end of 2019 [36, 37], has since spread to 213 countries and territories (<https://covid19.who.int/>). Given the novelty of the virus, the immunological susceptibility of the population, and the lack of a proven therapeutic or vaccine, the response toolbox of public health authorities has been limited to non-pharmaceutical interventions, such as recommending hand-washing and more stringent hygienic measures, or imposing social distancing measures, travel restrictions, and population confinement via stay-at-home orders [13, 22–26, 28–32]. Different countries, and often even different regions within each country, have adopted varying degrees of mobility restriction measures in an attempt to contain or at least slow down the spread. However, the effect of these measures on the temporal evolution of the epidemics varies significantly across geographical regions. The main reason behind such variability is likely to be that mobility itself is a multi-faceted phenomenon showing diverse characteristics at different

spatiotemporal scales. Indeed, long-range mobility is mainly driven by air transportation, but restrictions to international flights have shown limited utility in mitigating the propagation of infectious diseases unless they are applied very early and in a comprehensive manner [19, 21, 24]. At a more granular level—within countries, between provinces or states—transportation modes include train and road traffic, in addition to air travel, while at an even finer scale—within cities—vehicular traffic, pedestrian, bike, and public transportation modes are predominant [10, 38]. In particular, the unique mixture of different transportation modes at an urban level and spatial organization of activities and residential areas creates specific mobility fingerprints.

We start with an overview of how lockdowns affect mobility and epidemic spreading at a global scale. Fig. 1a explores the connection between mobility reduction and the maximum incidence  $I_{\max}$  (the maximum number of new daily cases per-capita). The color-code used in the map reflects the division of the two-variable space displayed in the inset. Darker colors correspond to larger incidence peaks, and are therefore indicative of more severe impacts. Although the pandemic is still evolving as of this writing, some interesting trends are apparent. In some countries like Japan, South Korea, Sweden or parts of the US, the mobility reductions are in the

\*Electronic address: gghoshal@pas.rochester.edu

†Electronic address: jramasco@ifisc.uib-csic.es

‡Electronic address: sadilekadam@google.com

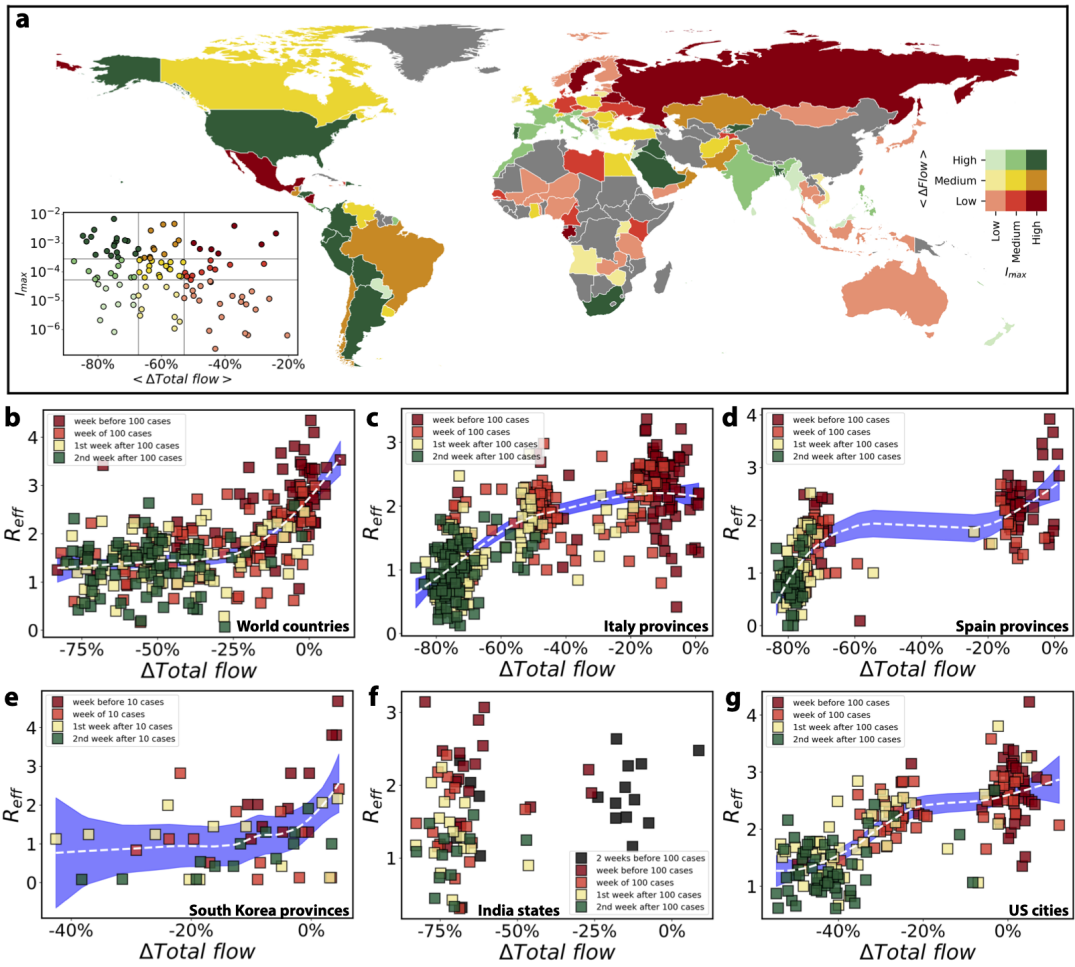


**FIG. 1: Impact of mobility restrictions on disease propagation at multiple scales** **a** Choropleth map of the highest mobility reduction versus the maximum incidence ( $I_{\max}$ ). The colors represent the division of the distribution of  $I_{\max}$  and the maximum travel reduction across countries (see inset). The data corresponds to the period January-June 2020. **b-g** Scatter plot of  $R_{\text{eff}}$  versus the corresponding mobility reduction one week before in terms of total flow for **b** countries (the baseline mobility is taken 5 weeks before the onset of 100 cases), **c** Italian provinces (baseline mobility: 2nd week of February), **d** Spanish provinces (baseline mobility: 2nd week of February), **e** South Korean provinces (baseline mobility: 2nd week of February), **f** Indian states (baseline mobility: 2nd week of March), and **g** US cities (baseline mobility: 3rd week of February). Due to the early lockdown in India, we also show data for 2 weeks before 100 cases. The dashed white line represent LOESS non-parametric fits, and the pale blue area corresponds to the 95% CI. Details on the mobility dataset are in Methods, Supplementary Table 1 for the epidemiological data sources and Supplementary Table 2 for the list of countries considered.

range 30-50% (detailed results by country are reported in Supplementary Fig. 1). However, the policies regarding testing and other protection measures are quite diverse and so is the epidemic impact. On the flip-side, countries like India, Italy and Spain, enforced mobility reductions by 80% in terms of total trip flows after the onset of the epidemics. The enforcement of lockdown policies produced both quantitative and qualitative differences in small- and medium-scale mobility patterns. At country scale, the trips suffering the most pronounced relative reduction are those in the medium-long distance range (see Supplementary Figs. 2-4). This means that the

different areas and cities of the countries are significantly less connected. In parallel, the weekly incidence of the disease is quite heterogeneous, and its association with the decrease of mobility is complex (see Supplementary Fig. 5).

The temporal evolution of the disease as a function of mobility reductions is shown in Fig. 1b-g. The key variable here is the effective reproduction number  $R_{\text{eff}}$ , computed as in [39, 40], capturing the transmissibility of the disease in the early stages of the local outbreak in each country. Each square of Fig. 1b represents a country and the colors correspond to different weeks

from the outbreak onset. Mobility restrictions cause a decrease of  $R_{\text{eff}}$ , and in about 2-3 weeks the effective reproduction number approaches 1 (the threshold of sustained spread) and the incidence reaches its peak. As the figure indicates, a decrease of internal country-level mobility between 25% – 50% is often associated with significantly reduced propagation. A similar behavior is observed at a finer resolution in Fig. 1c-f, where we show Italian, Spanish and South Korean provinces, as well as Indian states (see Supplementary Tables 3-6 for the list of provinces and states). There is still a noticeable reduction in  $R_{\text{eff}}$  when mobility restrictions are enforced, but its functional dependence on mobility changes. For instance, in Italy we observe the presence of a phased lockdown, with a relatively smooth decrease in mobility and  $R_{\text{eff}}$ . In this specific case, a nearly total lockdown corresponding to 80% reduction in flow was required to noticeably slow propagation down. For Indian states and Spanish provinces instead, we see an abrupt shift with a sudden transition from baseline mobility to 80% reduction, as an effect of a comprehensive and sudden lockdown. The case of South Korea is unique, mainly due to the government’s choice of concentrating resources on contact-tracing and large-scale testing, rather than on mobility restrictions. The connection between flow reduction and  $R_{\text{eff}}$  is therefore quite weak, as expected. Moving to even finer resolution, in Fig. 1g we plot the 50 largest metropolitan areas in the United States (See Supplementary Section 1 for a description of the OECD urban areas and Supplementary Table 7 for the list of US cities). The plot shows the same qualitative trends seen in Italy and Spain, although the comparatively lower mobility reductions implemented in the US caused the spread of the disease to continue for longer in many cities ( $R_{\text{eff}} > 1$  even two weeks after the first 100 cases).

The progression of the epidemic nationally is driven to a large extent by face-to-face contacts at the level of individual metropolitan areas. Hence, understanding how the spreading of a disease depends on the structural organization of a city and of its mobility patterns is of fundamental importance to adopt adequate and tailored containment strategies. At urban scale, a prior analysis revealed that the different areas of a city can be classified according to the level of mobility (trip outflows) in different levels of mobility hotspots as defined in [35]. When it comes to the internal organization of whole urban mobility patterns, cities can actually be classified in a spectrum between centralized-hierarchical and decentralized-sprawled [35]. In hierarchical cities, most flows (urban trips) occur between top mobility hotspots [33], whereas in sprawled cities flows are distributed more uniformly across the urban area. The level of centralization can be encapsulated in a metric  $\Phi$ , called the flow-hierarchy, that takes values between 0 and 1, so that higher values of  $\Phi$  correspond to more centralized cities (see Methods for details). Hierarchical cities are characterized by advanced levels of public transportation systems, higher population density,

and better indicators in terms of pollutant emissions per capita and health indices, whereas decentralized cities show higher level of private vehicle usage, lower population densities and sparser use of public transport. Given these differences in mobility profiles across cities, we next investigate the connection between the hierarchy and the COVID-19 propagation patterns.

The primary response to the early onset of the epidemic were mobility restrictions corresponding to stay-at-home measures, modifying the spatial patterns of urban mobility and disrupting most of the routes used by the virus to propagate, including daily commuting. In Fig. 2a-c, we show the spatial mobility layout for three cities arranged in increasing levels of centralization in their mobility structure: Atlanta ( $\Phi = 0.784$ ), Chicago ( $\Phi = 0.868$ ) and New York City NYC ( $\Phi = 0.909$ ). In each case, shown as red dots are the top mobility hotspots prior to lockdown. In the case of Atlanta, being a sprawled city, we see that the mobility hotspots are spread across the urban area, whereas Chicago and NYC being more hierarchical have their hotspots clustered in a centralized fashion. The new mobility hotspots that emerge after mitigation measures are shown as orange dots, whereas in blue, we show those areas that cease to be top hotspots. For hierarchical cities such as NYC or Chicago, while the original top hotspots remain in the reduced mobility phase, new areas of mobility activity emerge in a sprawled fashion, effectively distributing the mobility over larger parts of the city, thus reducing agglomeration. This effect is seen across the majority of American cities, whereby flows between pre-restriction hotspots are reduced (Supplementary Figure 6a). Instead, flows are sharply increased between the new sprawled hotspots (Supplementary Figure 6b). Indeed, in the case of Chicago, we see the emergence of suburban areas as hotspots, indicating that mobility is localized within smaller areas, and there is limited flow between locations. For the case of Atlanta, which is sprawled to begin with, a few mobility hotspots disappear, and others emerge, but there is little-to-no change in the spatial distribution. This can be seen in Supplementary Fig. 7, where we plot in decreasing order the fractional change in distance between hotspots due to the mobility restrictions finding that centralized cities tend to get more spread out, whereas in sprawled cities, mobility hotspots remain spatially separated, suggesting that mitigation measures have limited impact on the overall mobility structure.

In addition to the mobility-flows, we also have incidence curves for each administrative unit associated with the city (e.g., counties, supplementary tables 9-30 detail the list of counties considered per OCDE urban area). This allows us to run a granular analysis of the impact of lockdowns by investigating the extent to which specific areas of the city drive the epidemic spreading to other parts. To do so, we calculate the average Transfer Entropy,  $\langle \text{TE} \rangle$ , between the incidence curves for each subsets of the city (see Methods), and

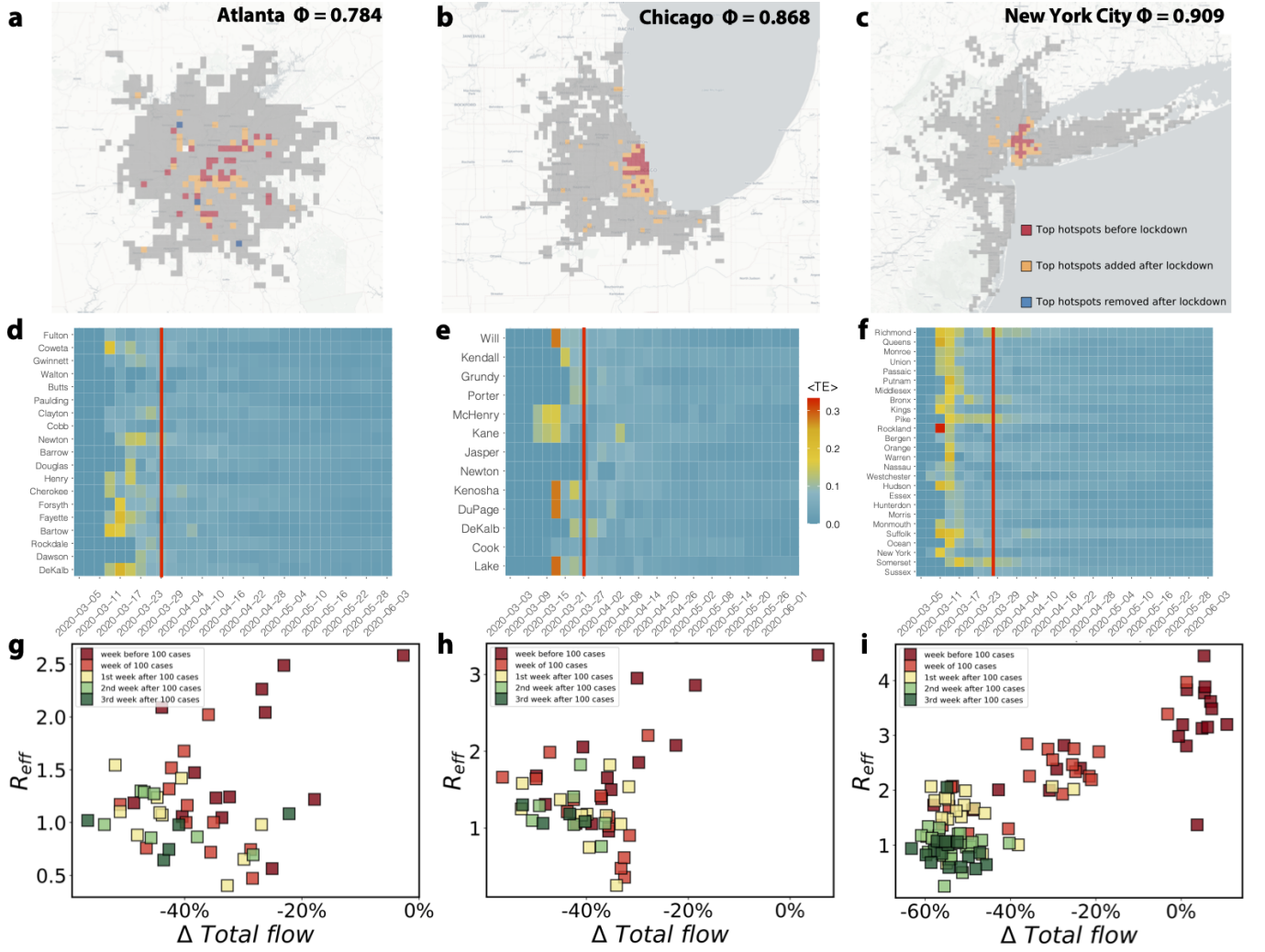


**FIG. 2: Types of cities and COVID-19 spreading.** Maps with the changes in mobility hotspots before and after the lockdown in three cities with different mobility hierarchy (higher  $\Phi$  indicates more centralized cities): **a-c** Atlanta, Chicago and New York City, respectively, in the week of February 2 for prelockdown mobility and the week April 5 for the postlockdown. **d-e** The average Transfer Entropy  $\langle S_T \rangle$ , capturing the influence of an administrative division (county) to drive infection-spread as a function of time. Vertical red lines mark the date of the official lockdown. After lockdown, the ability of a single region to drive infection spread dissipates, and the transmission evolves independently in each area. **g-i** The temporal evolution of the effective reproduction number before and after lockdown versus the mobility change one week before. Each symbol represents a county of the city. While sprawled cities like Atlanta have regions responding independently, in centralized New York City, we see a clear synchronized and monotonically decreasing reduction in  $R_{\text{eff}}$  as a function of mobility reduction.

in Fig. 2d-f plot the results as a matrix whose rows correspond to the administrative sub-unit, and columns correspond to weeks, starting from the onset of 100 cases, to the first week of June. The elements in the matrix are color-coded by the value of  $\langle \text{TE} \rangle$ . For all three cities, a few regions drive the spreading of the infection before lockdown, although the strength of the driving is stronger on average in NYC and Chicago compared to Atlanta (results for four other cities are reported in Supplementary Fig. 8). Once lockdown is initiated (marked as vertical red lines), the

driving becomes diffused, indicating the predominance of localized spreading in sub-regions with little influence on one another. The localization in spreading appears in parallel to the equivalent phenomenon in mobility, with a relative increase in self-flows and a decrease of inter-area flows in the administrative units (Supplementary Fig. 9). While the influence of each administrative unit on infection-spreading dissipates in a similar fashion, there is a key difference in how they are synchronized in terms of their response to mobility-mitigation. In Fig. 2g-i, we plot  $R_{\text{eff}}$  as a function of mobility reduction in each city

with points corresponding to sub-units and colored by time-period. While in Atlanta we see that each region more or less responds independently in terms of reducing transmission, for the case of Chicago we begin to see a pattern emerging, that becomes clear when looking at NYC where the various regions are clustered temporally and reduce transmission in a monotonically decreasing fashion with mobility-reduction.

These patterns generalize beyond the three cities. In Fig. 3a we plot  $R_{\text{eff}}$  in the early stages of the pandemic (three weeks after onset of 100 cases) as a function of the baseline  $\Phi$  for the top 22 metropolitan areas in the United States by number of counties with populations greater than two million inhabitants (full list of cities and their corresponding  $\Phi$  listed in Supplementary Table 8). There is a clear connection between transmissibility and mobility hierarchy, with hierarchical cities having an increased spread of the disease at the onset. Indeed NYC being the most hierarchical city in the United States, had a 50% higher value of  $R_{\text{eff}}$  than sprawled ones such as Cincinnati, Charlotte and Atlanta. This increased transmissibility is also reflected in the extent of the spread of the disease as measured by plotting  $I_{\text{max}}$  against  $\Phi$  in Fig. 3b. Cities can be separated into those that have already experienced a peak in the incidence curve (Northeastern and Midwestern cities, colored in yellow), and those which are still at the early phases of the pandemic (Southern and Western cities, in red). Restricting to cities where the pandemic is already well-established, we see a clear trend whereby hierarchical cities have a much wider outbreak as compared to sprawled ones. Stronger mitigation strategies manifest in those places where the outbreak is wide-spread [41], and a relation between mobility reduction and  $\Phi$  emerges as can be seen in Fig. 3c where we find that NYC, San Francisco and Boston reduce mobility by around 60%, whereas on the other end of the spectrum, Cincinnati, Minneapolis, Atlanta or Charlotte decrease mobility by around 40%. The connection between mobility reduction and reduced transmission is also far more pronounced: plotting the Pearson correlation between the reduction in  $R_{\text{eff}}$  and the corresponding change in total flow, the week before, as a function of  $\Phi$ , indicates that hierarchical cities seem significantly more responsive to mitigation measures (Fig. 3d). In order to check the robustness of our results with respect to the uncertainties in the epidemic data, we further confirm them using other data source in Supplementary Fig. 11.

The empirical results (Figs. 2 and 3) suggest that centralized cities experience faster and more widespread outbreaks as compared to sprawled ones. However, mobility restrictions and lockdowns in those cities are comparatively more effective. To confirm these findings, while removing potential confounding factors (population sizes, densities and spatial distribution, variation in type and timing of lockdowns, or noise in the data), we implement a metapopulation SEIR model of COVID-19

driven by empirical mobility flows before and after mitigation measures. The model uses a metapopulation framework, with S2 cells as geographical units connected by the network of mobility flows before the initiation of mitigation measures. We assign populations to S2 cells in proportion to the sum of their out- and self-flows. Furthermore, we assume that flows represent primarily commuting trips, and displacements outside the resident cells are followed by returns after a period of 8 hours. Previous research indicates that a substantial fraction of residents in areas as counties and municipality are not represented in commuting flows, and therefore we enforce that only 40% of residents in each cell travel (inside or out) [42]. Cities in this idealized configuration maintain their empirical  $\Phi$ , this design has the effect of scaling flows by a constant factor, without altering the network structure or the relative ranking of cell outflows.

To produce instances of a single city with different values of  $\Phi$ , we reshuffle a portion of randomly selected links by picking a new destination at random while maintaining the link-weights. This procedure creates multiple realizations of the city, preserving the population distribution and densities, as well as the total number of trips along with the number of destinations per origin. To simulate the effect of lockdowns, we replace the pre-lockdown empirical mobility network with the post-lockdown version once the fraction of infected individuals in the population reaches a threshold  $P_{\text{th}}$ . The mobility is reduced according to the empirical trip decrease in every cell, and a fraction  $X_S$  of susceptible individuals are considered as non-interacting [43–45]. The parameter  $P_{\text{th}}$  controls the time of the lockdown, while  $X_S$  determines its severity. (See Methods for a detailed description of the model and the values of relevant epidemic parameters.)

We begin by checking whether the model can reproduce the trend in Fig. 3a. The equivalent plot for three representative cities is shown in Fig. 4a, where we extract  $R_{\text{eff}}$  from the incidence curves of the simulations. The onset is set at  $10^4$  accumulated cases and  $\langle R_{\text{early}} \rangle$  is averaged over three weeks after onset, as done for the empirical data. The  $R^2$  for each individual city ranges from 0.95 – 0.97 indicating a clear signal for the transmissibility increasing with centralization. When measuring the correlation for the three cities collectively, confounding factors such as differences in population density and mobility distributions emerge, and  $R^2$  decreases to 0.63 in order of magnitude agreement with that seen for Fig. 3a obtained aggregating 22 different cities. Similar to that seen for Fig. 3b, we also reproduce the observation of the peak incidence  $I_{\text{max}}$  being monotonic in  $\Phi$  as shown in Fig. 4b. This is reflected in the final size of the outbreak (Fig. 4c) and the time taken to reach the peak incidence (Supplementary Figure 12), with more centralized cities experiencing stronger transmission, faster spread and wider prevalence in the population. These attributes in combination can rapidly overwhelm hospital capacity as well as the

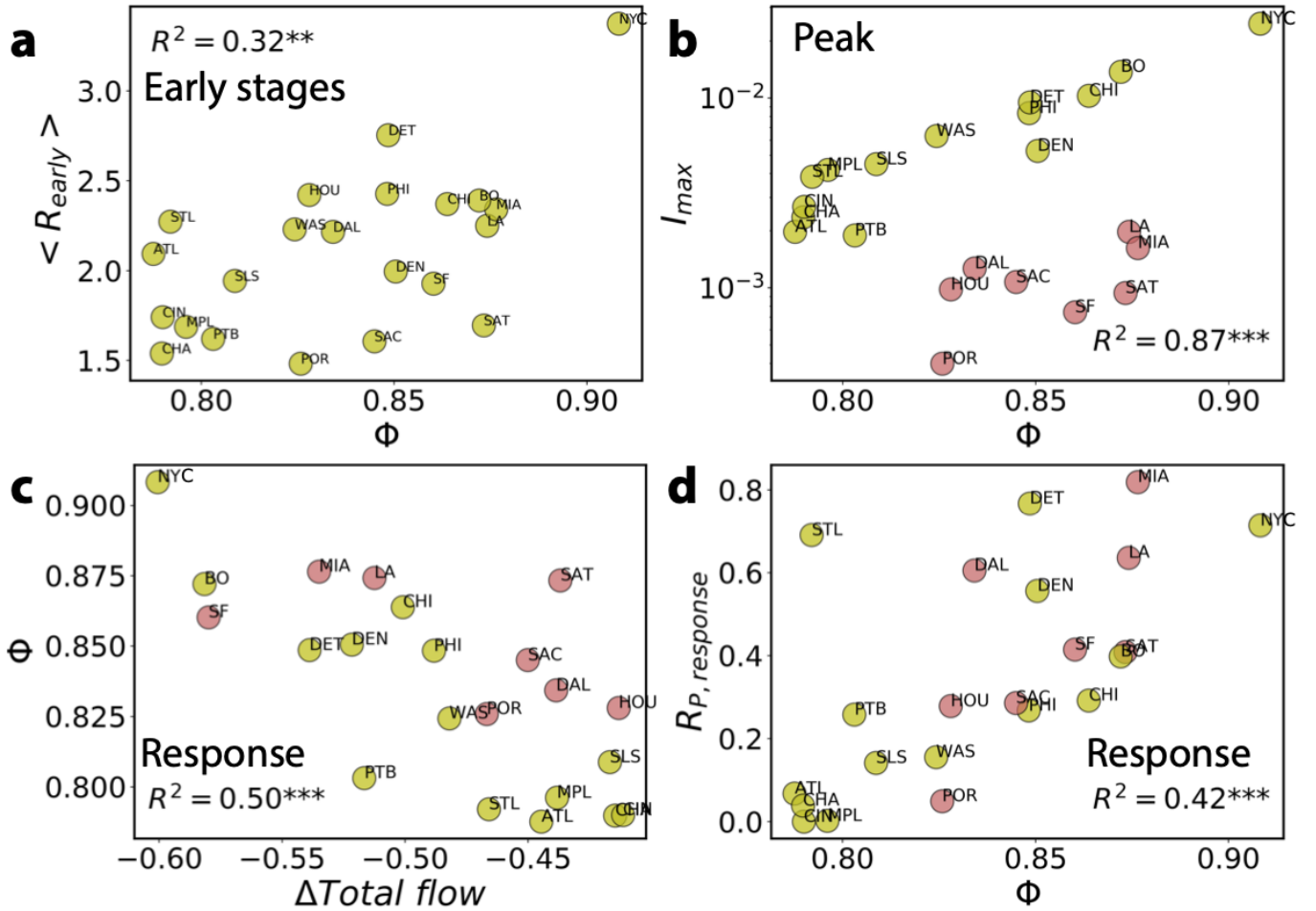


FIG. 3: **Connecting hierarchy with epidemic features and mitigation efforts.** Shown are the top 22 US cities by number of counties with more than two million inhabitants until June 14, 2020. **a** Average  $R_{\text{eff}}$  over three weeks after the onset of 100 cases as a function of  $\Phi$ . Initial transmission increases with centralization. **b** Accumulated number of new cases per capita two weeks before the maximum incidence  $I_{\text{max}}$ . Cities in pale yellow have already peaked, while infections continue to grow in those marked in red. The figure suggests the extent of spread is strongly correlated with centralization. In **c**,  $\Phi$  versus relative decrease in total flow. Mobility reductions are much more drastic in centralized cities. **d** Synchronization of mobility reduction and contagion spread among city counties measured through the Pearson coefficient of plots as those shown in Fig. 2 g-i for Atlanta, Chicago and NYC. Response to mitigation is more sensitive in cities with higher  $\Phi$ . (The equivalent figures for all 22 cities are shown in Supplementary Fig. 10). These results were obtained with data from the New York Times (Supplementary Table 1). We show the equivalent plots using an alternative data source, USAFacts, in Supplementary Fig. 11.

healthcare system at large, and is indeed what was seen in hierarchical cities such as NYC, London and Milan.

On the other hand, Fig. 3d suggests that cities with higher  $\Phi$  largely achieved a better reduction in transmission with lockdown measures. To simulate this, in Fig. 4d we plot the final size of the pandemic by instituting an 80% reduction in interactions ( $X_s = 0.8$ ) with the lockdown coming into effect at  $P_{\text{th}} = 5 \times 10^{-3}$ . Remarkably we see an inversion of the curve as compared to Fig. 4c with the trends now reversed; the final size of the pandemic is *lower* in cities with higher  $\Phi$  and is decreased by an order of magnitude as compared to

the scenario with no mitigation. The inversion of the curve resulted from a rather strong lockdown, so in Fig. 4e we show the case for a softer lockdown with  $X_s = 0.4$ ; here we see the same trend with  $\Phi$  as in the case with no lockdown, however, the size of the outbreak is reduced by a factor of five. In addition the time taken to institute mobility restriction measures is a crucial parameter, and in Fig. 4f, we show the case for an earlier (but still soft) lockdown with  $X_s = 0.4$  and  $P_{\text{th}} = 10^{-3}$ , finding a further decrease by a factor of three in the pandemic size. In terms of assessing the effect of different flavors of lockdowns, the connection between the



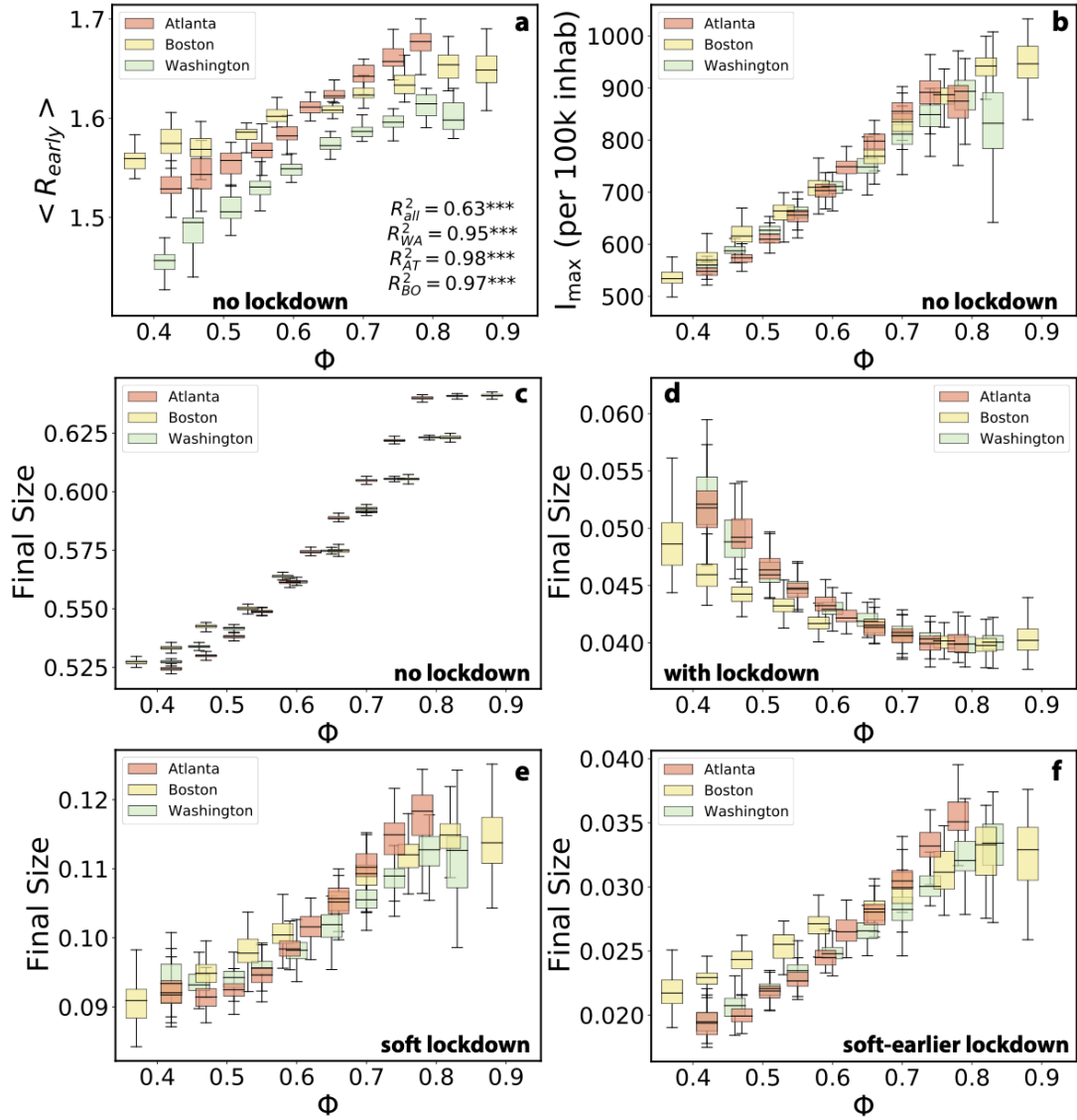


FIG. 4: **Modeling disease spread by type of city.** Results of a metapopulation model using the S2 cells as basic geographical units. Simulations are run in each city with different values of  $\Phi$ , obtained by the randomization procedure described in the text. Each box reflects 100 runs and displays the median, quartiles, the 5% and 95% confidence intervals. In **a**,  $R_{\text{eff}}$  in the early stages, averaged over three weeks after the onset of  $10^4$  cases as a function of  $\Phi$ , as in Fig. 3a. The peak incidence  $I_{\text{max}}$  is shown in **b**, and the final epidemic size in **c** both as a function of  $\Phi$ . All three panels correspond to the baseline mobility before lockdown. In **d-f** we show the pandemic size for three different lockdown scenarios: a strong lockdown,  $X_s = 0.8$ , for  $P_{\text{th}} = 5 \times 10^{-3}$ ; a soft lockdown,  $X_s = 0.4$ , at the same prevalence, and finally a soft but earlier lockdown  $X_s = 0.4$  and  $P_{\text{th}} = 10^{-3}$ .

size of the outbreak and its dependence on  $\Phi$ , is in general a complex function of the epidemiological parameters, the extent of mobility reduction and the distribution of flows. In Supplementary Figs. 13-15, we explore aspects of this interdependence for different values of  $R_0$  and  $X_S$ , confirming that when lockdown measures are enforced in time and in strength, centralized cities while being more susceptible, outperform or do at least as well as sprawled cities in mitigating the outbreak.

In summary, we studied how mobility restrictions

in urban areas affect the propagation of an infectious disease. We leveraged a massive global dataset that captures aggregate flows of populations around the globe in a consistent way since pre-pandemic times all the way to the most recent week. In a previous work, we had shown that hierarchical cities have better indicators in terms of the use of public transportation, walking, emissions per-capita and health indicators. However, their mobility structure favors spreading of infectious diseases in terms of speed and extent of the

contagions. At the same time, lockdown and travel restriction measures can lead to better outcomes in more hierarchical cities. From a policy-making point of view, it seems prudent to deploy robust early warning systems within hierarchical cities in particular. Furthermore, it is effective to enforce mitigation measures as early and as thoroughly as possible, given that the time-to-response is particularly crucial in hierarchical cities within or near an epidemic outbreak. Sprawled cities, with their distributed mobility and less connected outbreaks, have a larger window of time within which to enforce policy measures, yet even so, the intensity of response is important to reduce the final number of cases. These findings, while presented in the context of COVID-19, are also applicable to other potential infectious diseases. These results shed new light on the ongoing debate on the best design for cities, balancing between the multiplier effects that lead to socio-economic development against their susceptibility to threats such as pandemics.

## Methods

**Mobility data sets.** The mobility flows are sourced from the Google COVID-19 Aggregated Mobility Research Dataset, containing anonymized trips aggregated over users who have turned on the Location History setting, which is off by default. This is similar to the data used to show how busy certain types of places are in Google Maps, helping identify when a local business tends to be the most crowded. The dataset aggregates flows of populations between S2 cells (<https://github.com/google/s2geometry>) of approximately 5 km<sup>2</sup>. To produce this dataset, machine learning is applied to logs data to automatically segment it into semantic trips [35]. To provide strong privacy guarantees, all trips were anonymized and aggregated using a differentially private mechanism [46] to aggregate flows over time. This research is done on the resulting heavily aggregated and differentially private data. No individual user data was ever manually inspected, only heavily aggregated flows of large populations were handled.

**Limitations.** The results should be interpreted in light of several limitations. First, the Google mobility data is limited to smartphone users who have opted in to Google's Location History feature. These data may not be representative of the population as whole, and furthermore their representativeness may vary by location. Importantly, these limited data are only viewed through the lens of differential privacy algorithms, specifically designed to protect user anonymity and obscure fine detail. Moreover, comparisons across rather than within locations are only descriptive since these regions can differ in substantial ways.

**Epidemic data sets.** The epidemic data has been downloaded from sources listed in the Data Availability statement and in Supplementary Table 1.

**Mobility flows in urban areas.** The flows are

incorporated in an Origin-Destination matrix  $\mathbf{T}(\mathbf{t})$ , whose elements  $T_{ij}(t)$  encode the trip flow at week  $t$  between the two spatial units  $i$  and  $j$ . The diagonal terms  $T_{ii}$  correspond to movements within the area. The geographical unit corresponds to S2 cells of 5 km<sup>2</sup>. The total flow of a territory is the sum of the trips over all the S2 cells present in the city,  $T = \sum_{i,j} T_{ij}$ . In general, the relative trip-flow change between two timestamps  $t_1$  and  $t_2$  is calculated as  $(T(t_1) - T(t_2)) / T(t_2)$ . Note that when we estimate the reduction after lockdown,  $t_2$  refers to the mobility prior to the restrictions and  $t_1$  after the lockdown.

**Hierarchical structure of urban mobility.** To calculate  $\Phi$ , a hotspot level is assigned to each geographical unit (S2 cells), using a recurrent Lorenz curve as explained in Ref. [35]. Once every cell  $i$  is assigned a level  $L_i$ , trip flows between cells are aggregated as:

$$S_{\ell m} = \frac{\sum_{i < j} T_{ij} \delta(L_i, \ell) \delta(L_j, m)}{\sum_{i < j} T_{ij}} \quad (1)$$

where  $\ell$  and  $m$  are the levels and  $\delta(x, y)$  is the Kronecker delta. The flows  $S_{\ell m}$  are normalized by the total flow in the city. Self-flows within cells are not considered when calculating  $S_{\ell m}$ . With these definitions, the flow hierarchy  $\Phi$  is calculated according to

$$\Phi = \sum_{\ell, m} S_{\ell m} \{ \delta(\ell, m) + \delta(\ell, m - 1) + \delta(\ell - 1, m) \}. \quad (2)$$

## Calculation of driving between incidence curves.

In order to quantify the driving in the spreading between different areas of a city, we calculated the transfer entropy [47] between the time series of the disease incidence at the county (borough) level for time windows of increasing sizes. Starting from the first reported case to the latest available data (in most cases, the first week of June 2020, see the Supplementary Information for details on the epidemiological data). For each time window, the driving each administrative unit  $i$  had over the others is calculated as the average transfer entropy  $\langle \text{TE} \rangle_i = 1/N \sum_j \text{TE}_{ij}$  between the incidence time series of unit  $i$  and all the other units  $j$ , with  $N$  the number of administrative units in the city. The transfer entropy was evaluated using the *RTransferEntropy* library (<https://cran.r-project.org/web/packages/RTransferEntropy/vignettes/transfer-entropy.html>) in R, that also provides an estimation of the statistical significance of the results.

**SEIR metapopulation model.** The model is structured in a meta-population framework with Susceptible S, Exposed E, Infected I and Recovered R compartments and taking as basic spatial units the S2 cells provided by the mobility data. The whole population of the city  $P$  is distributed among the cells  $i$ , according to  $p_i = P(\sum_j T_{ij})/T$  where the index  $j$  runs over all cells including  $i$  and  $T$  corresponds to the total trips of the city. In the model without travel restrictions,



40% of the population of every cell  $i$  moves and selects their destination proportional to outflow  $T_{ij}$  from  $i$  to the other cells  $j$  (including  $T_{ii}$ ). The choice of a 40% mobility has been made in accordance with previous research, where it has been shown that for commuting flows, only a fraction of the population actively moves [11, 42]. Also note that non-moving individuals are not excluded from the epidemic dynamics but interactions occur inside their cell of residence. To incorporate commuting flows inside the epidemic dynamics, we followed a classical approach for metapopulation models with recurrent mobility [11, 42, 48]: introducing an effective force of infection for individuals residing at cell  $j$ , defined as  $\lambda_j$ .  $\lambda_j$  accounts for both the force of infection seen by an individual inside their residence cell  $\lambda_{jj}$  and while commuting to other cells  $\lambda_{ji}$  and can be calculated as

$$\lambda_j = \frac{\lambda_{jj}}{1 + \sigma_j/\tau} + \sum_{i \in v(j)} \frac{\lambda_{ji}\sigma_{ji}/\tau}{1 + \sigma_j/\tau} \quad (3)$$

where  $\sigma_j$  represents the travel rate of individuals in  $j$ ,  $\sigma_{ji}$  the travel rate between cells  $j$  and  $i$  while  $\tau$  accounts for the time usually spent outside the home cell during a working day ( $\tau^{-1} \sim 1/3$  day) and the sum runs over all the neighbors  $i$  of cell  $j$ ,  $v(j)$ . Finally,  $\lambda_{jj}$  and  $\lambda_{ji}$  are calculated as:

$$\lambda_{ji} = \frac{\beta}{N_j^*} \left( I_{ji} + \sum_{l \in v(j)} I_{lj} \right) \frac{S_{ji}}{S_i} \quad (4)$$

where  $\beta$  is the per contact infection rate,  $N_j^*$  is the effective population of  $j$  having into account commuting and the subscripts in  $I_{ij}$  (resp  $S_{ij}$ ) refer to the infected (susceptible) visitors from  $i$  in  $j$  (for a detailed derivation of  $\lambda_j$  and  $\lambda_{ji}$  see section 4.3 of [42]).

**Effect of mobility restrictions and stay-at-home orders.** To model the effect of lockdowns on mobility, we need to consider that mobility flows change in both magnitude and destination in response to the restrictions. With reductions that can reach up to 80% reduction of flows compared to baseline levels. In the metapopulation model and for sake of simplicity, for each city only two mobility networks have been extracted from the Google COVID-19 Aggregated Mobility Research Dataset: one considering a typical day prior to restrictions  $T_{ij}$  and another after restrictions have been imposed,  $L_{ij}$ . The total trips per cell  $i$  are then  $T_i = \sum_j T_{ij}$  and  $L_i = \sum_j L_{ij}$ . As for the normal mobility regime, where we impose that the 40% of population of each cell will move with destinations proportional to  $T_{ij}$ , during travel restrictions we assume that flows and destinations are chosen according to the new mobility matrix  $L_{ij}$ . Since travel flows in matrix  $\mathbf{L}$  are usually smaller than flows in  $\mathbf{T}$ , the total reduction in mobility is  $L_i/T_i$ , with the fraction of individuals traveling in the system  $0.4 (L_i/T_i)$ . In addition, it is important to note that during stay-at-home orders part of the population remained isolated or only interacted with individuals in their

household; not participating in the global spreading process directly. This effect has been modeled in the literature [43–45] by including a fraction  $X_S$  of susceptible individuals who do not participate in the infection process. In the main text,  $X_S$  is fixed at 0.8 with further values explored in Fig. 4e and f and in Supplementary Figs. 14–16. Finally, in order to model the fact that restrictive measures are enforced when outbreaks are discovered in the city, we assume that both travel restrictions and stay-at-home orders are imposed once the prevalence of the disease reached a certain threshold  $P_{th}$ , equal for all the cities considered. Unless otherwise specified, the particular parameters selected for the model are: the infectivity per contact  $\beta = 0.4 \text{ days}^{-1}$ , the average time spent as infectious  $t_I = \mu^{-1} = 3.8$  days and average time as exposed  $t_E = 3.7$  days.

### Acknowledgments

We thank Aaron Schneider, Aaron Stein, Ahmed Aktay, Alvin Raj, Amy Chung-Yu Chou, Andrew Oplinger, Ashley Zlatinov, Blaise Aguera y Arcas, Bryant Gipson, Charina Chou, Christopher Pluntke, Damien Desfontaines, Eric Tholome, Ewa Dominowska, Gregor Rothfuss, Iz Conroy, Janel Thamkul, Janet Whiteman, Jason Freidenfelds, Jeff Dean, Karen Lee Smith, Katherine Chou, Leeron Morad, Lizzie Dorfman, Marlo McGriff, Mia Vu, Michael Howell, Paul Eastham, Rif Saurus, Rishi Bal, Royce Wilson, Ruth Alcantara, Shawn O'Banion, Stephanie Cason, Thomas Roessler, Vivien Hoang, Yanning Zhang, Xue Ben and Brian Dickinson for their support and guidance.

M.M. is funded by the Conselleria d'Innovació, Recerca i Turisme of the Government of the Balearic Islands and the European Social Fund with grant code FPI/2090/2018. J.A., M.M., S.M. and J.J.R. also acknowledge funding from the project Distancia-COVID (CSIC-COVID-19) of the CSIC funded by a contribution of AENA, from the Spanish Ministry of Science and Innovation, the AEI and FEDER (EU) under the grant PACSS (RTI2018-093732-B-C22) and the Maria de Maeztu program for Units of Excellence in R&D (MDM-2017-0711). A.B. and V.N. acknowledge support from the UK EPSRC New Investigator Award Grant No. EP/S027920/1. GG, SH and SM acknowledge support from from NSF Grant IIS-2029095 and the US Army Research Office under Agreement Number W911NF-18-1-0421. A.K. is supported by the National Defense Science and Engineering Graduate Fellowship through the Department of Defense.

### Author contributions

G.G., S. Meloni, V.N., J.J.R. and A.S. developed the concepts and designed the study. A.B., S.H., A.K., M.M.

and S. Mimar analyzed the data. A.S. computed and provided the mobility map data. J.A., S. Meloni and J.J.R. developed the model. J.A. performed the model simulations. G.G., M.M., S. Meloni, J.J.R. and A.S. contributed to the work methodology. G.G., M.M., S. Meloni, V.N. and J.J.R wrote the paper. G.G., S. Meloni, J.J.R. and A.S. coordinated the study. All authors read, edited, and approved the final version of the paper. The authors are listed in alphabetical order.

### Data and code availability statement

The Google COVID-19 Aggregated Mobility Research Dataset used for this study is available with permission from Google LLC.

Covid data sources:

World: <https://www.ecdc.europa.eu/en/>

publications-data/download-todays-data-geographic-distribution-covid-19-cases-worldwide

Italy: <https://github.com/pcm-dpc/COVID-19>

USA: New York Times <https://github.com/nytimes/covid-19-data> and USAFacts <https://usafacts.org/visualizations/coronavirus-covid-19-spread-map/>

Spain: <https://github.com/montera34/escovid19data>

South Korea: <https://www.kaggle.com/marcuswingen/analysis-of-covid-19-data-from-south-korea>

India: <https://www.kaggle.com/sudalairajkumar/covid19-in-india/data#>

The code to calculate the flow hierarchy in cities is available in the following link: <https://mygit.katolaz.net/aleix/flow-hierarchy>.

- 
- [1] A. Flahault and A.-J. Valleron, Mathematical Population Studies **3**, 161 (1992).
  - [2] R. F. Grais, J. H. Ellis, and G. E. Glass, European Journal of Epidemiology **18**, 1065 (2003).
  - [3] L. Hufnagel, D. Brockmann, and T. Geisel, Procs. Nat. Acad. Sci. U.S.A. **101**, 15124 (2004).
  - [4] J. S. Brownstein, C. J. Wolfe, and K. D. Mandl, PLoS Medicine **3**, e401 (2006).
  - [5] V. Colizza, A. Barrat, M. Barthélemy, and A. Vespignani, Procs. Nat. Acad. Sci. U.S.A. **103**, 2015 (2006).
  - [6] V. Colizza, A. Barrat, M. Barthelemy, A.-J. Valleron, and A. Vespignani, PLoS Medicine **4** (2007).
  - [7] A. Tatem, Z. Huang, A. Das, Q. Qi, J. Roth, and Y. Qiu, Parasitology **139**, 1816 (2012).
  - [8] F. Finger, T. Genolet, L. Mari, G. C. de Magny, N. M. Manga, A. Rinaldo, and E. Bertuzzo, Procs. Nat. Acad. Sci. U.S.A. **113**, 6421 (2016).
  - [9] Q. Zhang, K. Sun, M. Chinazzi, A. P. y Piontti, N. E. Dean, D. P. Rojas, S. Merler, D. Mistry, P. Poletti, L. Rossi, et al., Procs. Nat. Acad. Sci. U.S.A. **114**, E4334 (2017).
  - [10] H. Barbosa, M. Barthelemy, G. Ghoshal, C. R. James, M. Lenormand, T. Louail, R. Menezes, J. J. Ramasco, F. Simini, and M. Tomasini, Physics Reports **734**, 1 (2018).
  - [11] D. Balcan, V. Colizza, B. Gonçalves, H. Hu, J. J. Ramasco, and A. Vespignani, Procs. Natl. Acad. Sci. U.S.A. **106**, 21484 (2009).
  - [12] M. Gilbert, G. Pullano, F. Pinotti, E. Valdano, C. Poletto, P.-Y. Boëlle, E. d’Ortenzio, Y. Yazdanpanah, S. P. Eholie, M. Altmann, et al., The Lancet **395**, 871 (2020).
  - [13] M. U. Kraemer, C.-H. Yang, B. Gutierrez, C.-H. Wu, B. Klein, D. M. Pigott, L. Du Plessis, N. R. Faria, R. Li, W. P. Hanage, et al., Science **368**, 493 (2020).
  - [14] M. Mazzoli, D. Mateo, A. Hernando, S. Meloni, and J. J. Ramasco, medRxiv p. 2020.05.09.20096339 (2020).
  - [15] B. Rader, S. Scarpino, A. Nande, A. Hill, R. Reiner, D. Pigott, B. Gutierrez, M. Shrestha, J. Brownstein, M. Castro, et al., medRxiv p. 2020.04.15.20064980 (2020).
  - [16] N. M. Ferguson, D. A. Cummings, S. Cauchemez, C. Fraser, S. Riley, A. Meeyai, S. Iamsirithaworn, and D. S. Burke, Nature **437**, 209 (2005).
  - [17] T. D. Hollingsworth, N. M. Ferguson, and R. M. Anderson, Nature Medicine **12**, 497 (2006).
  - [18] J. M. Epstein, D. M. Goedecke, F. Yu, R. J. Morris, D. K. Wagener, and G. V. Bobashev, PLoS ONE **2**, e401 (2007).
  - [19] P. Bajardi, C. Poletto, J. J. Ramasco, M. Tizzoni, V. Colizza, and A. Vespignani, PLOS ONE **6**, e16591 (2011).
  - [20] S. Meloni, N. Perra, A. Arenas, S. Gómez, Y. Moreno, and A. Vespignani, Scientific Reports **1**, 62 (2011).
  - [21] C. Poletto, M. F. Gomes, A. P. y Piontti, L. Rossi, L. Bioglio, D. L. Chao, I. M. Longini, M. E. Halloran, V. Colizza, and A. Vespignani, Eurosurveillance **19**, 20936 (2014).
  - [22] H. Fang, L. Wang, and Y. Yang, Tech. Rep., National Bureau of Economic Research (2020).
  - [23] E. Pepe, P. Bajardi, L. Gauvin, F. Privitera, B. Lake, C. Cattuto, and M. Tizzoni, medRxiv p. 2020.03.22.20039933 (2020).
  - [24] M. Chinazzi, J. T. Davis, M. Ajelli, C. Gioannini, M. Litvinova, S. Merler, A. P. y Piontti, K. Mu, L. Rossi, K. Sun, et al., Science **368**, 395 (2020).
  - [25] A. Pan, L. Liu, C. Wang, H. Guo, X. Hao, Q. Wang, J. Huang, N. He, H. Yu, X. Lin, et al., Jama (2020).
  - [26] M. Gatto, E. Bertuzzo, L. Mari, S. Miccoli, L. Carraro, R. Casagrandi, and A. Rinaldo, Procs. Nat. Acad. Sci. U.S.A. **117**, 10484 (2020).
  - [27] S. Pei, S. Kandula, and J. Shaman, medRxiv p. 2020.05.15.20103655 (2020).
  - [28] N. Haug, L. Geyrhofer, A. Londei, E. Dervic, A. Desvars-Larrive, V. Loreto, B. Pinior, S. Thurner, and P. Klimek, medRxiv (2020).
  - [29] J. Dehning, J. Zierenberg, F. P. Spitzner, M. Wibral, J. P. Neto, M. Wilczek, and V. Priesemann, Science **369**, 160 (2020).
  - [30] B. F. Maier and D. Brockmann, Science **368**, 742 (2020).
  - [31] H. P. Melo, J. Henriques, R. Carvalho, T. Verma, J. P.

- da Cruz, and N. Araujo, arXiv preprint arXiv:2006.15724 (2020).
- [32] F. Schlosser, B. F. Maier, D. Hinrichs, A. Zachariae, and D. Brockmann, arXiv preprint arXiv:2007.01583 (2020).
  - [33] T. Louail, M. Lenormand, O. G. C. Ros, M. Picornell, R. Herranz, E. Frias-Martinez, J. J. Ramasco, and M. Barthelemy, *Scientific Reports* **4**, 5276 (2014).
  - [34] R. Ewing and S. Hamidi, *Journal of Planning Literature* **30**, 413 (2015).
  - [35] A. Bassolas, H. Barbosa-Filho, B. Dickinson, X. Dotiwalla, P. Eastham, R. Gallotti, G. Ghoshal, B. Gipson, S. A. Hazarie, H. Kautz, et al., *Nature Communications* **10**, 4817 (2019).
  - [36] P. Zhou, X.-L. Yang, X.-G. Wang, B. Hu, L. Zhang, W. Zhang, H.-R. Si, Y. Zhu, B. Li, C.-L. Huang, et al., *Nature* **579**, 270 (2020).
  - [37] F. Wu, S. Zhao, B. Yu, Y.-M. Chen, W. Wang, Z.-G. Song, Y. Hu, Z.-W. Tao, J.-H. Tian, Y.-Y. Pei, et al., *Nature* **579**, 265 (2020).
  - [38] L. Varga, A. Kovács, G. Tóth, I. Papp, and Z. Néda, *PLOS ONE* **11**, e0148913 (2016).
  - [39] M. Tizzoni, *Estimating covid-19's rt in real-time* (2020), URL <https://github.com/micheletizzoni/covid-19>.
  - [40] L. M. Bettencourt and R. M. Ribeiro, *PLoS ONE* **3** (2008).
  - [41] G. Pullano, E. Valdano, N. Scarpa, S. Rubrichi, and V. Colizza, medRxiv p. 2020.05.29.20097097 (2020).
  - [42] D. Balcan, B. Gonçalves, H. Hu, J. J. Ramasco, V. Colizza, and A. Vespignani, *Journal of Computational Science* **1**, 132 (2010).
  - [43] L. Di Domenico, G. Pullano, C. E. Sabbatini, P.-Y. Boëlle, and V. Colizza, medRxiv p. 2020.04.13.20063933 (2020).
  - [44] A. Aleta, D. Martin-Corral, A. Pastore y Piontti, M. Ajelli, M. Litvinova, M. Chinazzi, N. E. Dean, M. E. Halloran, I. M. Longini, S. Merler, et al., medRxiv p. 2020.05.06.20092841 (2020).
  - [45] A. Arenas, W. Cota, J. Gomez-Gardenes, S. Gómez, C. Granell, J. T. Matamalas, D. Soriano-Panos, and B. Steinegger, medRxiv p. 2020.03.21.20040022 (2020).
  - [46] R. Wilson, C. Y. Zhang, W. Lam, D. Desfontaines, D. Simmons-Marengo, and B. Gipson (2020).
  - [47] T. Bossomaier, L. Barnett, M. Harré, and J. T. Lizier, Cham: Springer International Publishing pp. 65–95 (2016).
  - [48] L. Sattenspiel and K. Dietz, *Mathematical Biosciences* **128**, 71 (1995).

# Supplementary Information

## Impact of urban structure on COVID-19 spread

J. Aguilar, A. Bassolas, G. Ghoshal, S. Hazarie, A. Kirkley, M. Mazzoli, S. Meloni,  
S. Mimar, V. Nicosia, J.J. Ramasco & A. Sadilek

### Table of Contents

<b>1</b>	<b>Geographical data</b>	<b>2</b>
<b>2</b>	<b>Epidemic data</b>	<b>2</b>
<b>3</b>	<b>Multiscale mobility reduction across countries</b>	<b>6</b>
<b>4</b>	<b>Mobility restrictions &amp; its effect on spreading</b>	<b>9</b>
<b>5</b>	<b>Flow hierarchy</b>	<b>15</b>
<b>6</b>	<b>The metapopulation model</b>	<b>19</b>

## 1 Geographical data

The city boundaries used throughout the study are the functional urban areas provided by the OECD [https://ec.europa.eu/eurostat/statistics-explained/index.php/Glossary:Functional\\_urban\\_area](https://ec.europa.eu/eurostat/statistics-explained/index.php/Glossary:Functional_urban_area).

## 2 Epidemic data

Country	URL	Description
World	<a href="https://ecdc.europa.eu/en/publications-data/">ecdc.europa.eu/en/publications-data/</a>	European Centre for Disease Prevention and Control
Italy	<a href="https://github.com/pcm-dpc/COVID-19">github.com/pcm-dpc/COVID-19</a>	Protezione Civile official monitoring of Covid cases
USA	<a href="https://github.com/nytimes/covid-19-data">github.com/nytimes/covid-19-data</a>	New York Times coverage of covid cases by counties
USA-2	<a href="https://usafacts.org/visualizations/coronavirus-covid-19-spread-map/">usafacts.org/visualizations/coronavirus-covid-19-spread-map/</a>	USAFacts alternative coverage of covid cases by counties
Spain	<a href="https://github.com/montera34/escovid19data">github.com/montera34/escovid19data</a>	Independent coverage of covid cases
South Korea	<a href="https://kaggle.com/marcuswingen/analysis-of-covid-19-data-from-south-korea">kaggle.com/marcuswingen/analysis-of-covid-19-data-from-south-korea</a>	Official coverage from Korea Centers for Disease Control & Prevention
India	<a href="https://kaggle.com/sudalairajkumar/covid19-in-india/data20">kaggle.com/sudalairajkumar/covid19-in-india/data20</a>	Official coverage from Indian Ministry of Health & Family Welfare

Supplementary Table 1: **Covid data sources.**

Countries	Countries	Countries	Countries
Afghanistan	Finland	Luxembourg	Saudi Arabia
Angola	France	Malaysia	Senegal
Argentina	Gabon	Mali	Singapore
Australia	Georgia	Malta	Slovakia
Austria	Germany	Mauritius	Slovenia
Bahrain	Ghana	Mexico	South Africa
Bangladesh	Greece	Moldova	South Korea
Belarus	Guatemala	Mongolia	Spain
Belgium	Haiti	Morocco	Sri Lanka
Bolivia	Honduras	Myanmar	Sweden
Bosnia and Herzegovina	Hungary	Netherlands	Switzerland
Brazil	India	New Zealand	Taiwan
Bulgaria	Indonesia	Nicaragua	Tajikistan
Burkina Faso	Iraq	Niger	Thailand
Cambodia	Ireland	Nigeria	Togo
Cameroon	Israel	Norway	Trinidad and Tobago
Canada	Italy	Oman	Turkey
Chile	Jamaica	Pakistan	Uganda
Colombia	Japan	Panama	Ukraine
Costa Rica	Jordan	Paraguay	United Arab Emirates
Croatia	Kazakhstan	Peru	United Kingdom
Czechia	Kenya	Philippines	United Republic of Tanzania
Denmark	Kuwait	Poland	United States of America
Dominican Republic	Kyrgyzstan	Portugal	Uruguay
Ecuador	Latvia	Qatar	Venezuela
Egypt	Lebanon	Romania	Vietnam
El Salvador	Libya	Russia	Yemen
Estonia	Lithuania	Rwanda	Zambia

Supplementary Table 2: **Table of world countries considered in Figure 1.**



Province	Province	Province	Province	Province
Agrigento	Catania	La Spezia	Pavia	Siracusa
Alessandria	Catanzaro	Latina	Perugia	Sondrio
Ancona	Chieti	Lecce	Pesaro e Urbino	Sud Sardegna
Aosta	Como	Lecco	Pescara	Taranto
Arezzo	Cosenza	Livorno	Piacenza	Teramo
Ascoli Piceno	Cremona	Lodi	Pisa	Terni
Asti	Crotone	Lucca	Pistoia	Torino
Avellino	Cuneo	Macerata	Pordenone	Trapani
Bari	Enna	Mantova	Potenza	Trento
Barletta-Andria-Trani	Fermo	Massa-Carrara	Prato	Treviso
Belluno	Ferrara	Matera	Ragusa	Trieste
Benevento	Firenze	Messina	Ravenna	Udine
Bergamo	Foggia	Milano	Reggio di Calabria	Varese
Biella	Forl�-Cesena	Modena	Reggio nell'Emilia	Venezia
Bologna	Forl�-Cesena	Monza e della Brianza	Rieti	Verbano-Cusio-Ossola
Bolzano/Bozen	Frosinone	Napoli	Rimini	Vercelli
Brescia	Genova	Novara	Roma	Verona
Brindisi	Gorizia	Nuoro	Rovigo	Vibo Valentia
Cagliari	Grosseto	Oristano	Salerno	Vicenza
Caltanissetta	Imperia	Padova	Sassari	Viterbo
Campobasso	Isernia	Palermo	Savona	
Caserta	L'Aquila	Parma	Siena	

Supplementary Table 3: **Table of Italian provinces considered in Figure 1.**

Provinces	Provinces	Provinces	Provinces
A Coru�a	Cantabria	La Rioja	Salamanca
�lava	Castell�n	Las Palmas	Santa Cruz de Tenerife
Albacete	Ceuta	Le�n	Segovia
Alicante	Ciudad Real	Lleida	Sevilla
Almer�a	C�rdoba	Lugo	Soria
Asturias	Cuenca	Madrid	Tarragona
�vila	Girona	M�laga	Teruel
Badajoz	Granada	Melilla	Toledo
Baleares	Guadalajara	Murcia	Valencia
Barcelona	Guip�zcoa	Navarra	Valladolid
Burgos	Huelva	Ourense	Vizcaya
C�ceres	Huesca	Palencia	Zamora
C�diz	Ja�n	Pontevedra	Zaragoza

Supplementary Table 4: **Table of Spanish provinces considered in Figure 1.**

Provinces	Provinces	Provinces
Busan	Gwangju	Jeollabuk-do
Chungcheongbuk-do	Gyeonggi-do	Jeollanam-do
Chungcheongnam-do	Gyeongsangbuk-do	Sejong
Daegu	Gyeongsangnam-do	Seoul
Daejeon	Incheon	Ulsan
Gangwon-do	Jeju-do	

Supplementary Table 5: **Table of South Korean first-tier administrative divisions considered in Figure 1.**

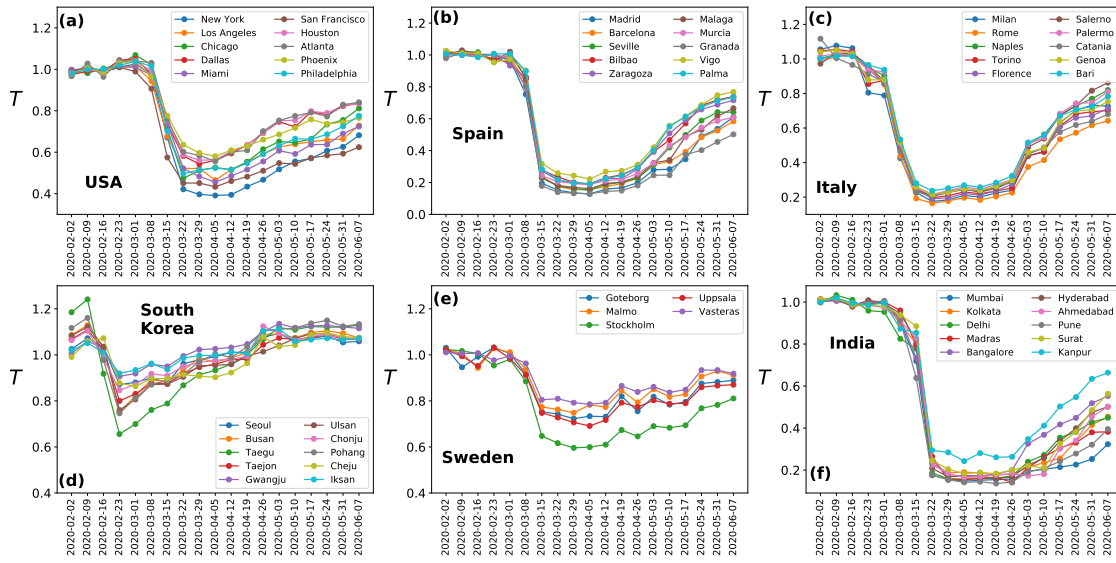
States	States	States	States
Andhra Pradesh	Haryana	Odisha	Uttarakhand
Assam	Jammu and Kashmir	Punjab	West Bengal
Bihar	Jharkhand	Rajasthan	
Chandigarh	Karnataka	Tamil Nadu	
Chhattisgarh	Kerala	Telangana	
Delhi	Madhya Pradesh	Tripura	
Gujarat	Maharashtra	Uttar Pradesh	

Supplementary Table 6: **Table of Indian States considered in Figure 1.**

Cities	Cities	Cities	Cities
Atlanta	Hartford	New Orleans	San Diego
Austin	Houston	New York	San Francisco
Boston	Indianapolis	Oklahoma	Seattle
Charlotte	Jackson	Orange	St. Louis
Chicago	Jacksonville	Philadelphia	Tulsa
Cincinnati	Jefferson	Phoenix	Virginia Beach
Columbus	Las Vegas	Pima	Wake
Cuyahoga	Los Angeles	Pittsburgh	Washington
Dallas	Memphis	Portland	
Davidson	Miami	Richmond	
Denver	Milwaukee	Sacramento	
Detroit	Minneapolis	Salt Lake	
Fresno	New Haven	San Antonio	

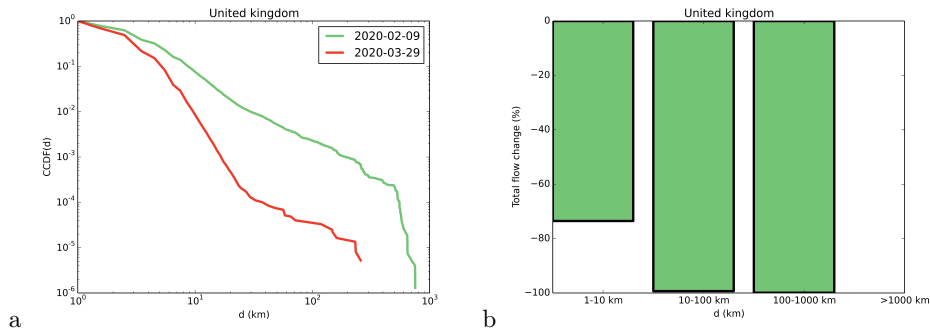
Supplementary Table 7: **Table of US cities considered in Figure 1.**

### 3 Multiscale mobility reduction across countries

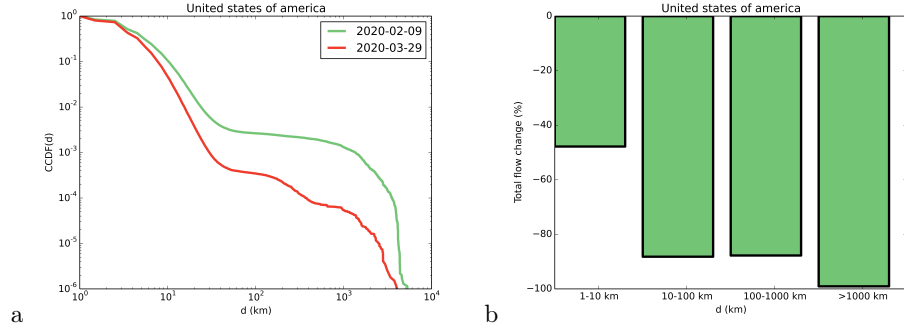


Supplementary Figure 1: **Changes in mobility in 10 major cities of 6 countries that applied different mitigation strategies** . Curves in panels a-f represent temporal change in mobility compared to the baseline average mobility in February.

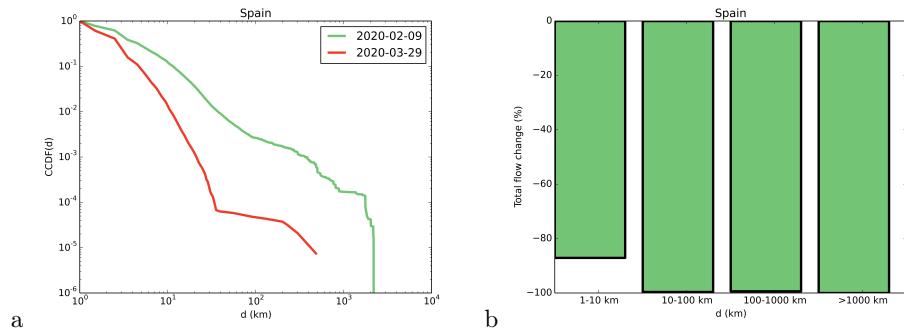
The reduction of mobility has an uneven impact across the different scales in a city. As we show in Supplementary Figure 2 for the United Kingdom, the longest trips beyond the city scale incur a more drastic decrease in mobility, which can be observed in both the CCDF and the associated bar plot. Similar plots where the same trend can be observed are shown in Supplementary Figures 3 and 4 for the United States and Spain, respectively.



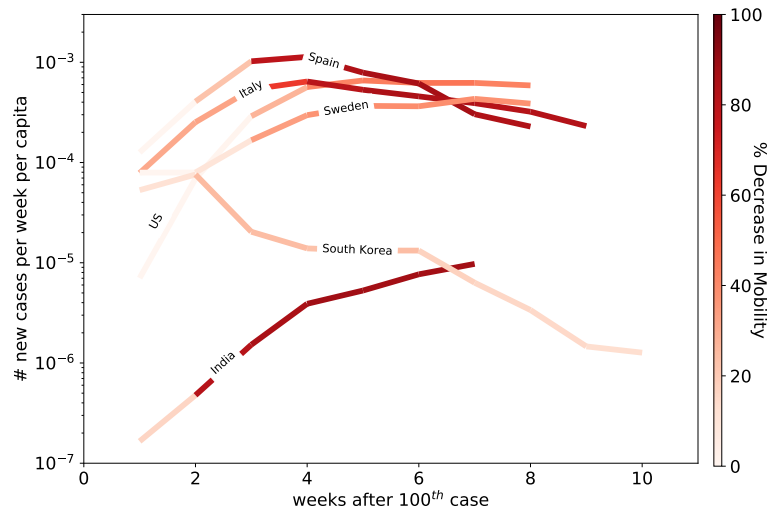
Supplementary Figure 2: **Reduction of mobility at different scales in the United Kingdom**. **a** Complementary cumulative distribution of trip distances in 09-02-2020 and in 29-03-2020. **b** Percentage of change in total flow as a function of the distance of the trips.



Supplementary Figure 3: **Reduction of mobility at different scales in the United States of America.** **a** Complementary cumulative distribution of trip distances in a 09-02-2020 and in 29-03-2020. **b** Percentage of change in total flow as a function of the distance of the trips.

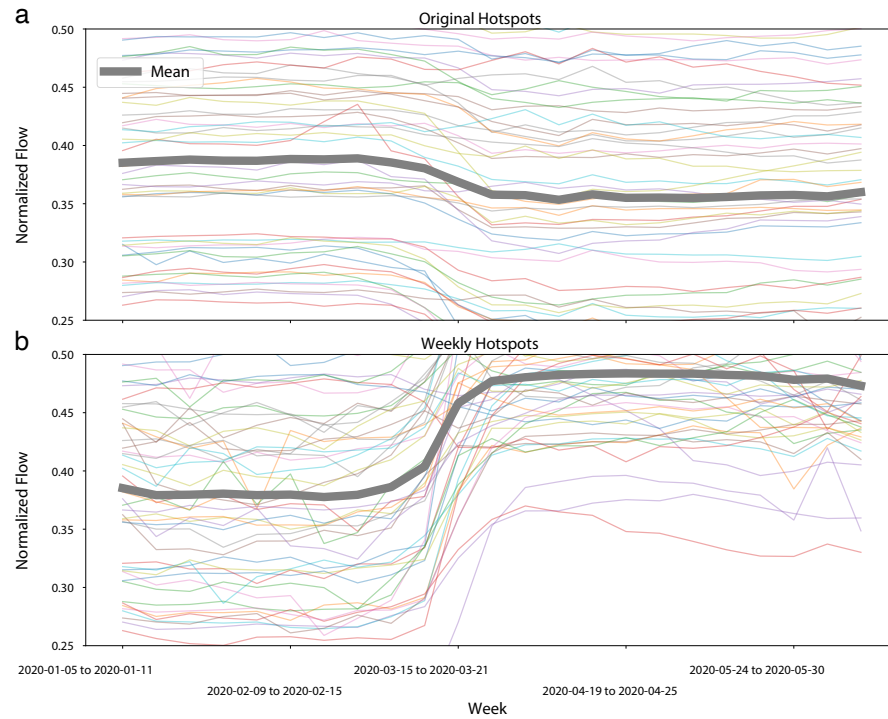


Supplementary Figure 4: **Reduction of mobility at different scales in Spain.** **a** Complementary cumulative distribution of trip distances in a 09-02-2020 and in 29-03-2020. **b** Percentage of change in total flow as a function of the distance of the trips.



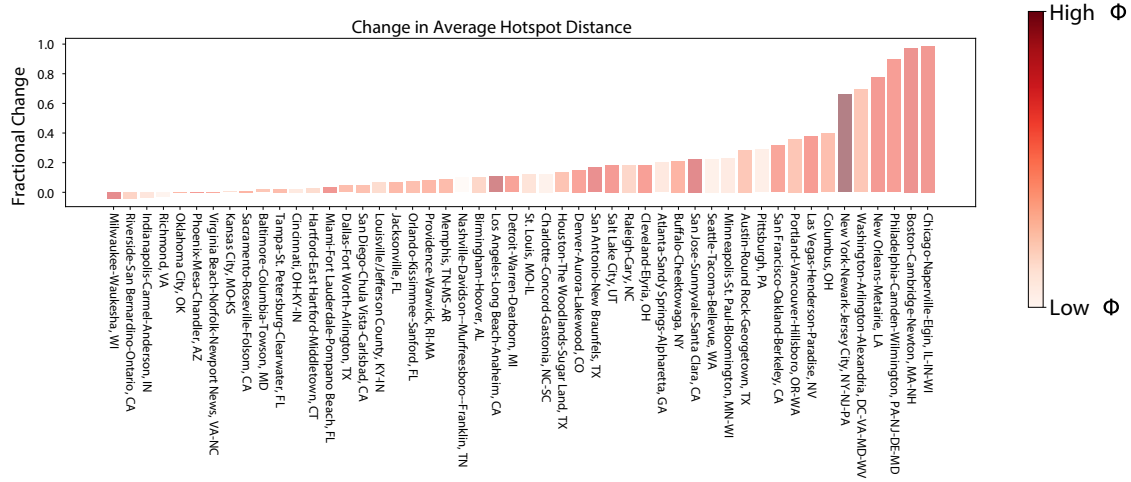
Supplementary Figure 5: **Number of new cases per capita and mobility change in 6 countries starting from the week after 100<sup>th</sup> case.** Curves are colored according to the percentage mobility change in each country relative to the week after reaching 100 cases.

## 4 Mobility restrictions & its effect on spreading

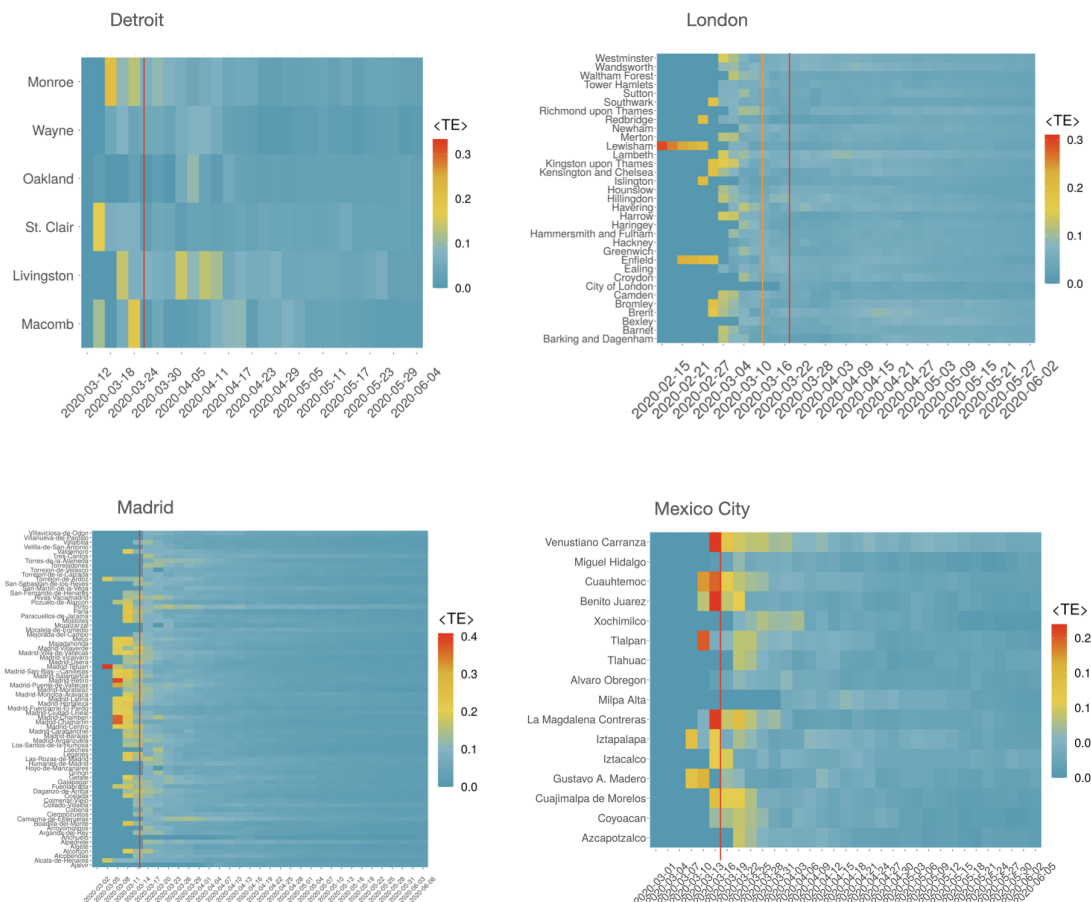


Supplementary Figure 6: **Flows to hotspots.** **a** The normalized flow to inflow hotspots calculated at the week of January 5 2020, over time, for the top 50 CBSAs in the US (only curves between .25 and .5 shown, with the mean in gray.) We see that the epidemic conditions cause the flows to the original hotspots to decrease, indicating a shift in travel destinations. **b** The normalized flow to hotspots calculated at each week. We see that the flows increase, contrary to **a**, suggesting that people concentrate their flows in different areas in response to the epidemic.

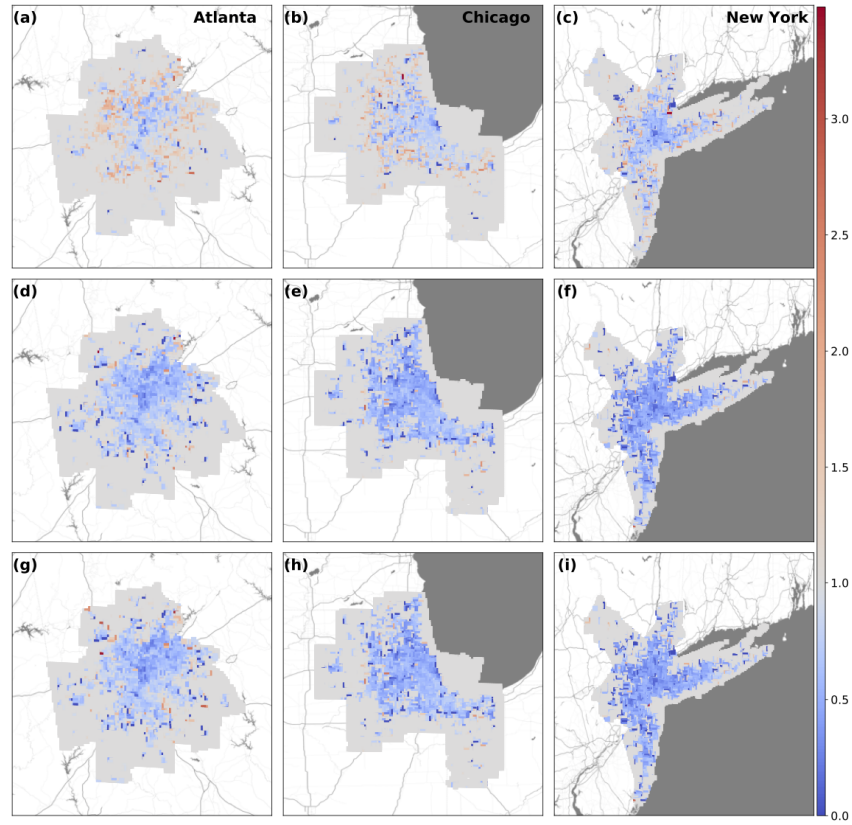




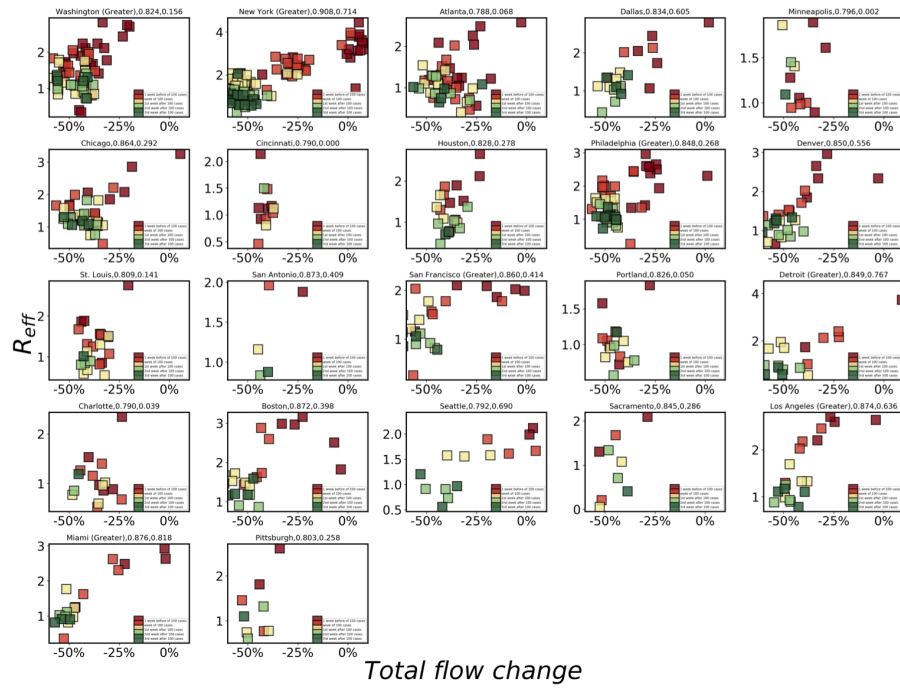
Supplementary Figure 7: **Distances between hotspots.** Fractional change in average hotspot distance from the week of January 5 to the week of June 7 for the top 50 CBSAs in the US, colored by the hierarchy as of January 5.



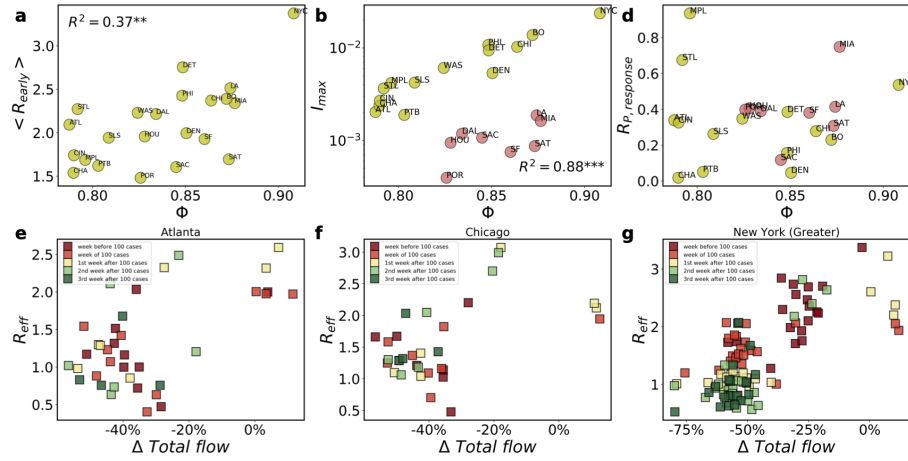
Supplementary Figure 8: **Average Transfer Entropy  $\langle TE \rangle$  for each administrative division (county or borough) with respect to the others as a function of time.** Shown are six different cities: Detroit, London, Madrid and Mexico city. Vertical red lines mark the date of the official lockdown. For London the orange line marks an advisory from the Prime Minister’s office to suspend all non essential activities, which occurred one week before the lockdown (red line).



Supplementary Figure 9: **Localization of flow in three cities with different mobility hierarchy.** Flow distributions in the month of April in Atlanta, Chicago and New York are compared to the baseline mobility level in February. Cells with no flow change are colored grey and have mobility ratio 1. Mobility increase and decrease are illustrated by red and blue colors for cells with mobility ratio greater than and less than 1, respectively. Panels **a**, **b**, **c** represent self-flows, **d**, **e**, **f** represent in-flows, and **g**, **h**, **i** represent out-flows.



Supplementary Figure 10: **Reduction of  $R_{\text{eff}}$  versus relative reduction of total flow at the county level in USA Metro Areas.**  $R_{\text{eff}}$  versus total flow reduction in counties within the same city, measured from one week before the onset to three weeks after the onset.  $R_{\text{eff}}$  is taken with one week of delay with respect to mobility data. This data is used to measure the correlations shown in Figure 3 of the main paper. Only counties with more than 100 accumulated cases in the full observation period are shown.



Supplementary Figure 11: **Reproduction of Fig. 3 with alternative data.** The same panels of the Fig.3 of the main paper with data from USAFacts. **a** Average  $R_{\text{eff}}$  over three weeks after the onset of 100 cases as a function of  $\Phi$ . Initial transmission increases with centralization. **b** Maximum incidence  $I_{\text{max}}$  (infections per capita). Cities in pale yellow have already peaked, while infections continue to grow in those marked in red. The figure suggests the extent of spread is strongly correlated with centralization. In **d**, synchronization of mobility reduction and contagion spread among city counties measured through the Pearson coefficient of plots as those in panels **e-g**, which reproduce those of shown in Fig. 2 **g-i** of the main manuscript for Atlanta, Chicago and NYC. The panel Fig.3c is not reproduced because it is only based on mobility data and it does not change with the source of the COVID-19 case information.

## 5 Flow hierarchy

Supplementary Table 8: **Table of US metro areas (and their short names) considered in Figure 3 as function of  $\Phi$ .**

Metro Area	Shortening	$\Phi$	Metro Area	Shortening	$\Phi$
New York (Greater)	NYC	0.908	Dallas	DAL	0.834
Miami (Greater)	MIA	0.876	Houston	HOU	0.828
Los Angeles (Greater)	LA	0.874	Portland	POR	0.826
San Antonio	SAT	0.873	Washington (Greater)	WAS	0.824
Boston	BO	0.872	St. Louis	SLS	0.809
Chicago	CHI	0.864	Pittsburgh	PTB	0.803
San Francisco (Greater)	SF	0.860	Minneapolis	MPL	0.796
Denver	DEN	0.850	Seattle	STL	0.792
Detroit (Greater)	DET	0.849	Cincinnati	CIN	0.790
Philadelphia (Greater)	PHI	0.848	Charlotte	CHA	0.790
Sacramento	SAC	0.845	Atlanta	ATL	0.788

Supplementary Table 9: **Table of counties per OCDE metropolitan area for New York City.**

County	County	County	County
Bergen County	Bronx County	Essex County	Hudson County
Hunterdon County	Kings County	Middlesex County	Monmouth County
Monroe County	Morris County	Nassau County	New York County
Ocean County	Orange County	Passaic County	Pike County
Putnam County	Queens County	Richmond County	Rockland County
Somerset County	Suffolk County	Sussex County	Union County
Warren County	Westchester County		

Supplementary Table 10: **Table of counties per OCDE metropolitan area for Miami.**

County	County	County	County
Broward County	Martin County	Miami-Dade County	Palm Beach County

Supplementary Table 11: **Table of counties per OCDE metropolitan area for Los Angeles.**

County	County	County	County
Los Angeles County	Orange County	Riverside County	San Bernardino County

Supplementary Table 12: **Table of counties per OCDE metropolitan area for San Antonio.**

County	County	County	County
Atascosa County	Bandera County	Bexar County	Comal County
Frio County	Guadalupe County	Kendall County	Medina County
Wilson County			



Supplementary Table 13: **Table of counties per OCDE metropolitan area for Boston.**

County	County	County	County
Essex County	Middlesex County	Norfolk County	Plymouth County
Suffolk County			

Supplementary Table 14: **Table of counties per OCDE metropolitan area for Chicago.**

County	County	County	County
Cook County	DeKalb County	DuPage County	Grundy County
Jasper County	Kane County	Kendall County	Kenosha County
Lake County	McHenry County	Newton County	Porter County
Will County			

Supplementary Table 15: **Table of counties per OCDE metropolitan area for San Francisco.**

County	County	County	County
Alameda County	Contra Costa County	Marin County	San Benito County
San Francisco County	San Mateo County	Santa Clara County	

Supplementary Table 16: **Table of counties per OCDE metropolitan area for Denver.**

County	County	County	County
Adams County	Arapahoe County	Broomfield County	Clear Creek County
Denver County	Douglas County	Elbert County	Gilpin County
Jefferson County	Park County		

Supplementary Table 17: **Table of counties per OCDE metropolitan area for Detroit.**

County	County	County	County
Livingston County	Macomb County	Monroe County	Oakland County
St. Clair County	Wayne County		

Supplementary Table 18: **Table of counties per OCDE metropolitan area for Philadelphia.**

County	County	County	County
Bucks County	Burlington County	Camden County	Cecil County
Chester County	Delaware County	Gloucester County	Mercer County
Montgomery County	New Castle County	Philadelphia County	Salem County

Supplementary Table 19: **Table of counties per OCDE metropolitan area for Sacramento.**

County	County	County	County
El Dorado County	Placer County	Sacramento County	Yolo County

Supplementary Table 20: **Table of counties per OCDE metropolitan area for Dallas.**

County	County	County	County
Collin County	Cooke County	Dallas County	Denton County
Ellis County	Fannin County	Hood County	Hunt County
Johnson County	Kaufman County	Palo Pinto County	Parker County
Rains County	Rockwall County	Somervell County	Tarrant County
Van Zandt County	Wise County		

Supplementary Table 21: **Table of counties per OCDE metropolitan area for Houston.**

County	County	County	County
Austin County	Brazoria County	Chambers County	Colorado County
Fort Bend County	Galveston County	Harris County	Liberty County
Montgomery County	Polk County	San Jacinto County	Waller County

Supplementary Table 22: **Table of counties per OCDE metropolitan area for Portland.**

County	County	County	County
Clackamas County	Clark County	Columbia County	Cowlitz County
Multnomah County	Skamania County	Washington County	

Supplementary Table 23: **Table of counties per OCDE metropolitan area for Washington.**

County	County	County	County
Alexandria city	Anne Arundel County	Arlington County	Baltimore County
Baltimore city	Calvert County	Carroll County	Charles County
Clarke County	Culpeper County	District of Columbia	Fairfax County
Falls Church city	Fauquier County	Frederick County	Fredericksburg city
Harford County	Howard County	Jefferson County	Loudoun County
Montgomery County	Prince George's County	Prince William County	Rappahannock County
Spotsylvania County	St. Mary's County	Stafford County	Warren County

Supplementary Table 24: **Table of counties per OCDE metropolitan area for St. Louis.**

County	County	County	County
Jefferson County	Jersey County	Lincoln County	Madison County
Monroe County	St. Charles County	St. Clair County	St. Louis County
St. Louis city	Warren County		

Supplementary Table 25: **Table of counties per OCDE metropolitan area for Pittsburgh.**

County	County	County	County
Allegheny County	Washington County	Westmoreland County	

Supplementary Table 26: **Table of counties per OCDE metropolitan area for Minneapolis.**

County	County	County	County
Anoka County	Carver County	Chisago County	Dakota County
Hennepin County	Isanti County	Kanabec County	Pierce County
Ramsey County	Scott County	Sherburne County	St. Croix County
Washington County	Wright County		

Supplementary Table 27: **Table of counties per OCDE metropolitan area for Seattle.**

County	County	County	County
King County	Pierce County	Snohomish County	Thurston County

Supplementary Table 28: **Table of counties per OCDE metropolitan area for Cincinnati.**

County	County	County	County
Boone County	Bracken County	Butler County	Campbell County
Clermont County	Dearborn County	Gallatin County	Grant County
Hamilton County	Kenton County	Ohio County	Pendleton County
Warren County			

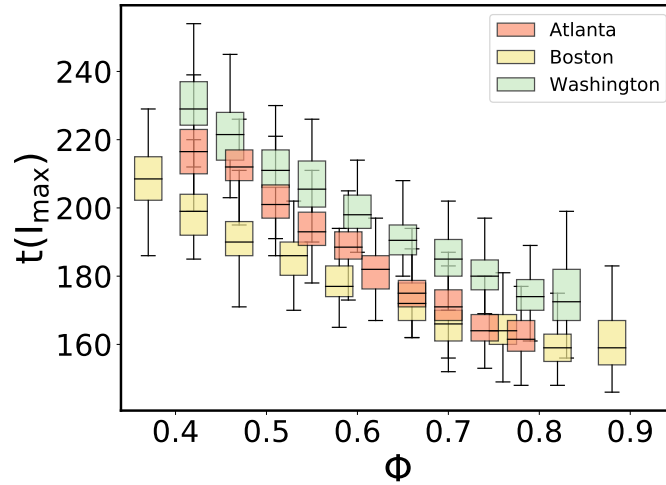
Supplementary Table 29: **Table of counties per OCDE metropolitan area for Charlotte.**

County	County	County	County
Cabarrus County	Gaston County	Mecklenburg County	Union County
York County			

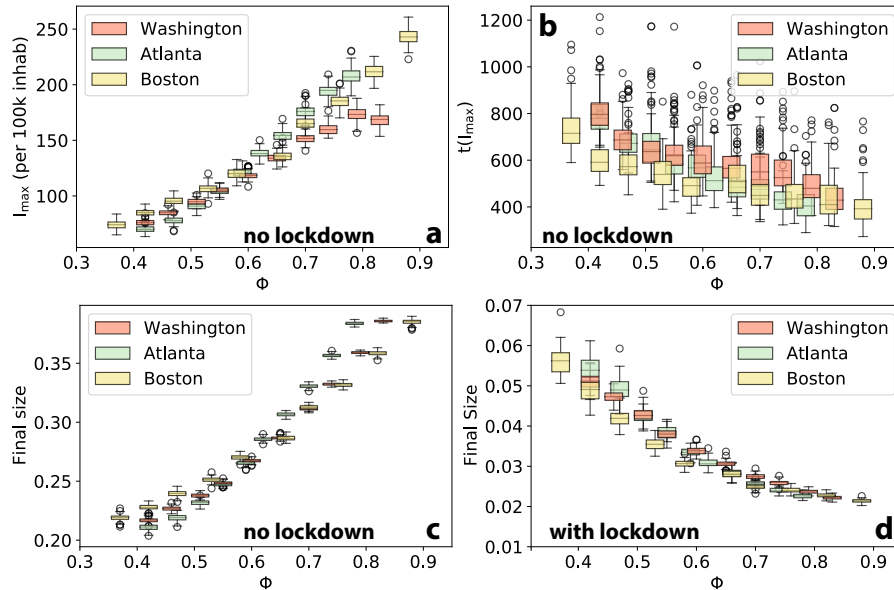
Supplementary Table 30: **Table of counties per OCDE metropolitan area for Atlanta.**

County	County	County	County
Barrow County	Bartow County	Butts County	Cherokee County
Clayton County	Cobb County	Coweta County	Dawson County
DeKalb County	Douglas County	Fayette County	Forsyth County
Fulton County	Gwinnett County	Henry County	Newton County
Paulding County	Rockdale County	Walton County	

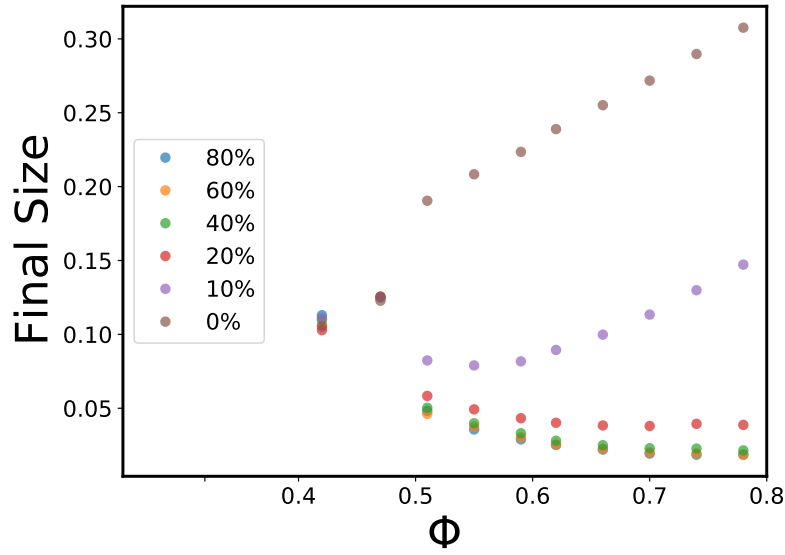
## 6 The metapopulation model



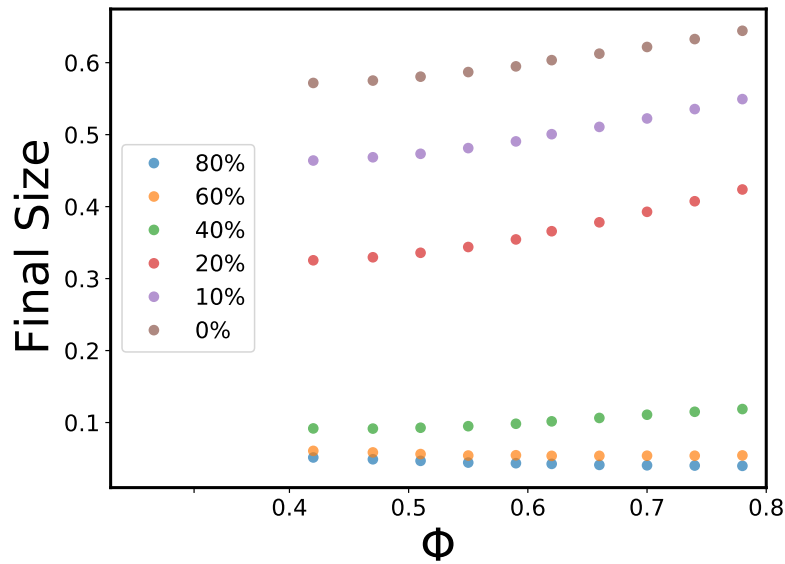
Supplementary Figure 12: **Relation between the time of the incidence peak and  $\Phi$ .** Simulations without lockdown and with the same parameters as in Fig. 4 of the main manuscript. The more hierarchical cities are, higher  $\Phi$ , the quicker the peak arrives.



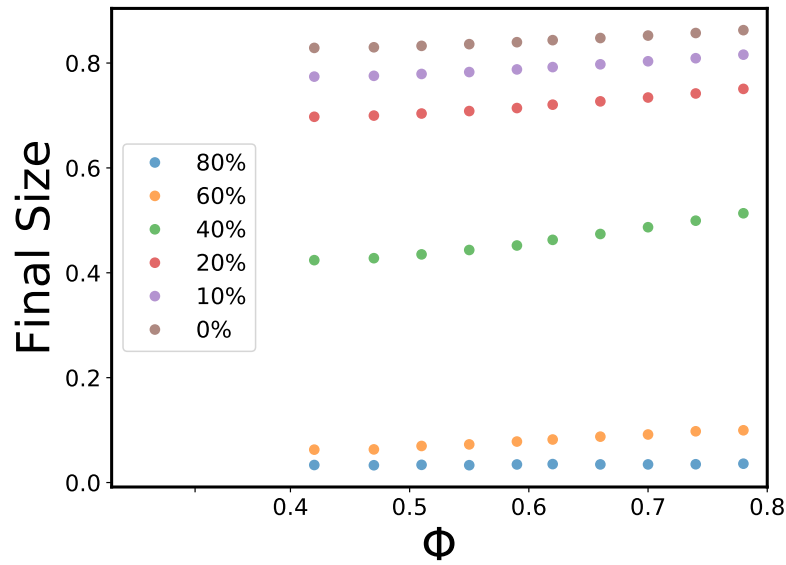
Supplementary Figure 13: **Model with  $R_0 \approx 1.2$ .** Simulations run with the same parameters as Fig. 4 of the main manuscript but decreasing the infectivity parameter  $\beta$  to obtain a reproduction number  $R_0 \approx 1.2$ . The panels without lockdown are: **a** the height of the peak of incidence, **b** the time of the peak and **c** the epidemic size, all as a function of  $\Phi$ . In **d**, the epidemic size versus  $\Phi$  for a simulation with lockdown  $X_S = 0.8$  and triggering the lockdown at a prevalence  $P_{th} = 5 \times 10^{-3}$ .



Supplementary Figure 14: **Model with  $R_0 \approx 1.2$ .** Simulations run with the same parameters as Fig. 4 but with  $\beta = 0.31 \text{ days}^{-1}$  inducing a reproduction number  $R_0 \approx 1.2$  for a city generated with the mobility network and total population of the Atlanta metropolitan area. The value of the epidemic size is explored as a function of  $\Phi$  for different values of  $X_S$  that are shown in the legend. In this way, it is possible to observe the inversion of the size versus  $\Phi$  curves for strong lockdowns. Given the low infectivity in this figure  $P_{th} = 10^{-3}$ .



Supplementary Figure 15: **Model with  $R_0 \approx 1.6$ .** Simulations run with the same parameters as Fig. 4 ( $\beta = 0.42 \text{ days}^{-1}$ ) producing a reproduction number  $R_0 \approx 1.6$  for a city generated with the mobility network and total population of the Atlanta metropolitan area. The value of the epidemic size is explored as a function of  $\Phi$  for different values of  $X_S$  that are shown in the legend. In this way, it is possible to observe the inversion of the size versus  $\Phi$  curves for strong lockdowns. As most of the panels of Figure 4,  $P_{th} = 5 \times 10^{-3}$ .



Supplementary Figure 16: **Model with  $R_0 \approx 2.3$ .** Simulations run with the same parameters as Fig. 4 but with  $\beta = 0.6 \text{ days}^{-1}$  inducing a reproduction number  $R_0 \approx 2.3$  for a city generated with the mobility network and total population of the Atlanta metropolitan area. The value of the epidemic size is explored as a function of  $\Phi$  for different values of  $X_S$  that are shown in the legend. In this way, it is possible to observe the inversion of the size versus  $\Phi$  curves for strong lockdowns. As most of the panels of Figure 4,  $P_{th} = 5 \times 10^{-3}$ .